indispensable for structure determination by NMR. BB-loop mutants of TICAM-1 and TICAM-2 are known to be dominant-negative and unable to form homotypic interactions (1, 2). Thus, we prepared P434H and C117H (P116H) mutants of the TICAM-1 and TICAM-2 TIR domains, respectively (Fig. 1*B*) [hereafter designated TICAM-1 P434H and TICAM-2 C117H (TICAM-2 P116H)] and analyzed their homotypic interactions using yeast two-hybrid experiments. Yeast two-hybrid experiments showed that the homotypic interaction is disrupted by the BB-loop mutation (Fig. 1*C*), consistent with previous reports (1, 2) and NMR observation of both wild types and BB-loop mutants (SI Text and Fig. S1).

NMR Structures of the TICAM-1 P434H and TICAM-2 C117H Mutants. The solution structures of the TICAM-1 P434H and TICAM-2 C117H mutants were determined based on distance and dihedral angle constraints. Structural statistics for the final 20 conformers of each protein are summarized in Table S1. The core structures, consisting of residues other than the BB-loops and N-terminal and C-terminal regions, were well defined. The root-mean-square-deviation (rmsd) of the core backbone atoms (Cα, N, C') of TICAM-1 P434H (395–427 and 442–527) and TICAM-2 C117H (83–110, 132–215) were 0.45 Å and 0.50 Å, respectively (Fig. 2 *A* and *B*). The global structures of both mutants were comprised of five parallel β-strands surrounded by six or seven α-helices and loops that connect β-strands and α-helices. Following the conventional nomenclature for TIR domains, the five strands in TICAM-1 were designated βA(397–400), βB(424–427), βC(451–455), βD (486–491), and βE(511–514), and the six helices in TICAM-1 were designated αA(406–419), αB(441–449), αC(462–474), αD (501–507), αE(520–528), and αE'(530–538) with a kink at residue 529 (Fig. 2*C*). Similarly, TICAM-2 C117H also contained five strands designated βA(81–85), βB(109–112), βC(134–138), βD(169–173), and βE(193–195) and seven α-helices, designated αA(90–101), αB(125–129), αC(142–152), αC'(156–161), αD (186–191), αE(202–210), and αE'(212–232) (Fig. 2*D*). In both structures, the conformation of the BB-loop was not well defined due to broadening of the NMR signals, resulting in insufficient NOE distance restraints. (Fig. 2 *A* and *B*).

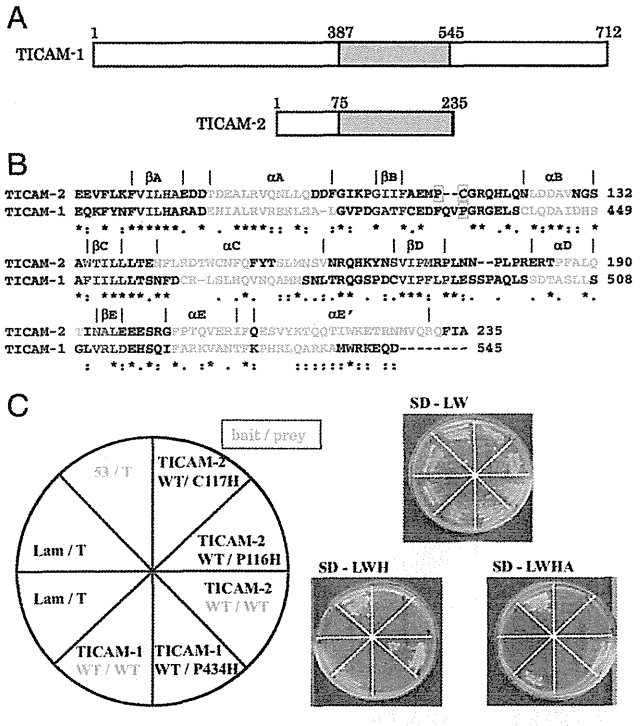

Fig. 1. Homotypic interaction of TICAM-1 and TICAM-2 TIR domains. (*A*) TIR domains of TICAM-1 and TICAM-2. The gray boxes represent the TIR domains of TICAM-1 and TICAM-2. (*B*) Sequence alignment of the TIR domains of human TICAM-1 and human TICAM-2. Amino acid residues involved in the β-sheet and α-helix are shown in blue and red, respectively. The residues on the BB-loop enclosed by a red line were substituted by His for the solution structure determination in this study. Numbers at the right side of the sequences correspond to the residue number in human TICAM-1 and TICAM-2. (*C*) Yeast two-hybrid analysis of homotypic interaction in TICAM-1 and TICAM-2. Pro434 of TICAM-1, Pro116 and Cys117 of TICAM-2 in the BB-loop were substituted by His residue. These mutants disrupted homotypic interaction of the TIR domain in TICAM-1 and TICAM-2. p53/T-antigen and Lamine/T-antigen were used as positive and negative controls in the yeast two-hybrid assay, respectively. SD-LW, SD-LWH, and SD-LWHA indicate a synthetic dropout medium lacking Leu and Trp, lacking Leu, Trp, and His, and that further lacking Ade, respectively.

Electrostatic surface potentials of TICAM-1 P434H and TICAM-2 C117H are shown in Fig. 2 *E* and *F*, respectively. TICAM-1 P434H has an extensive basic surface comprised of αE (Arg522, Lys523) and αE' (Lys529, Arg532, Arg536, Lys537, Arg541, Lys542). In contrast, TICAM-2 C117H has an extensive acidic surface comprised of the AA-loop (Glu87, Asp88, Asp89) and the αA-helix (Asp91, Glu92, Asp102, Asp103).

A Dali search (28) revealed that the structure of the TIR domain of TICAM-1 is most similar to that of TICAM-2, with a z-score of 9.6 and an rmsd of 3.8 Å for the structured region (Cα 122 atoms), followed by the TIR domains of TLR2 (z-score 9.2), TLR1 (z-score 8.8), TLR10 (z-score 8.7), IL-1RAPL (z-score 8.5), and MyD88 (z-score 7.5). A structural superposition was made to align the secondary structures and functionally important residues in TICAM-1, TICAM-2, and other TIR domains using the MATRAS program (29, 30) (Fig. S2). Intriguingly, the residues that form an extensive acidic surface in the TICAM-2 TIR domain and an extensive basic surface in the TICAM-1 TIR domain are not conserved in other TIR domains, suggesting that these residues might be responsible for specific interaction between TICAM-1 and TICAM-2.

Acidic Region of TICAM-2 and Basic Region of TICAM-1 Are Essential for Heterotypic Interaction. To investigate heterotypic interactions between the TICAM-1 and TICAM-2 TIR domains, further yeast two-hybrid experiments were carried out (31). Because previous studies showed that oligomerization of the TICAM-2 TIR domain is essential for its interaction with the TICAM-1 TIR domain (1, 2, 27), the wild-type TICAM-2 TIR domain was used as bait, and the TICAM-1 TIR domain mutants were used as prey. To search for residues that are essential for the interaction with TICAM-2, basic residues within TICAM-1 αE and αE'-helices were selected and mutated to alanine in the first round of two-hybrid experiments. The TICAM-1 mutants harboring the BB-loop mutation, P434H/R512A, P434H/K529A, and P434H/R532A, could interact with TICAM-2, but the mutants R522A/K523A and P434H/R522A/K523A could not (Fig. 3*A*). These results indicate that Arg522 and Lys523 of TICAM-1, but not Pro434, Arg512, Lys529, and Arg532, are crucial for direct interaction with TICAM-2, consistent with the observation that TICAM-1 oligomerization is not required for interaction with the TICAM-2 TIR domain. We designated the region involving Arg522 and Lys523 the "RK site." Actually, Pro434 is located on the opposite side of the RK site in TICAM-1, indicating that the homotypic and heterotypic interaction sites in the TICAM-1 TIR domain are distinct (Fig. 3*B*). Interestingly, the BB-loop mutant could still interact with wild-type TICAM-2, implying that monomeric TICAM-1 retains its ability to bind to the TIR domain of the TICAM-2 wild-type dimer.

After finding two basic residues in the TICAM-2 binding surface of TICAM-1, we searched for acidic residues in TICAM-2 that complemented the interaction. Arrays of two or three acidic residues from the TIR domain of TICAM-2 (E87/D88/D89 in the AA-loop, D91/E92 in the N-terminal side of the αA-helix, D102 / D103 in the C-terminal side of the αA-helix, D126/D127 in the αB-helix, and E197/E198 in the EE-loop) were substituted with alanine.

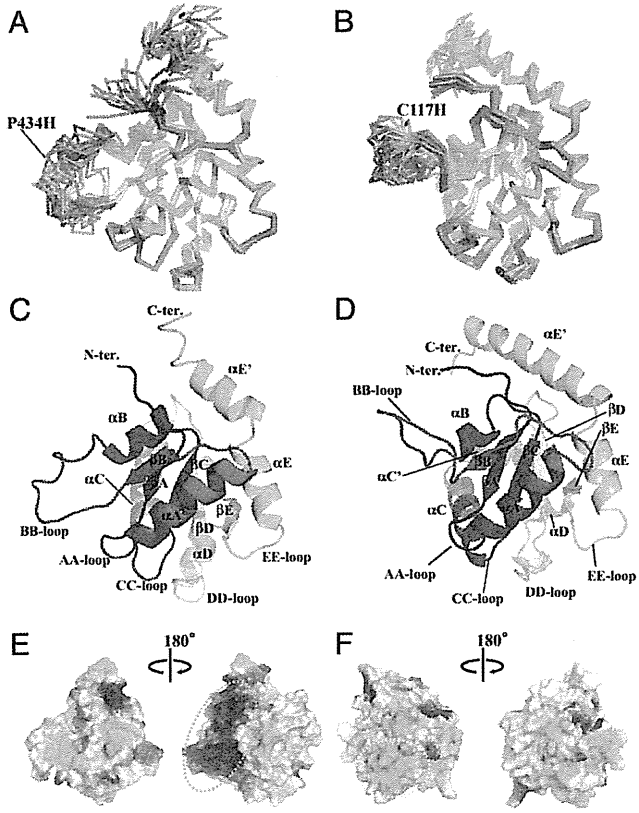

Fig. 2. Structures of the TICAM-1 and TICAM-2 TIR domains. (*A* and *B*) The overlay of the 20 lowest energy structures of the TIR domains of TICAM-1 and TICAM-2 determined by NMR. The backbone atoms (N, Cα, C') of polypeptides are drawn in wire model; β-sheets in yellow; α-helices in red. Pro434 of TICAM-1 and Cys117 of TICAM-2 in BB-loop are substituted with His, which are shown in orange and labeled. (*C* and *D*) The TIR domain of TICAM-1 (*C*) and TICAM-2 (*D*) in ribbon model. β-strands, α-helices, and the connecting loops are labeled after the conventional nomenclature of the TIR domain (9). (*E* and *F*) Electrostatic surface potential of the TIR domains of TICAM-1 (*E*) and TICAM-2 (*F*). Positive, negative, and neutral electrostatic surface potentials are presented in blue, red, and white, respectively. The electrostatic surface potential in *E* and *F*, *Left* is presented as the same orientation as shown in *A* (*C*) and *B* (*D*). The opposite surfaces are shown in *E* and *F*, *Right*. The basic surface in TICAM-1 TIR and the acidic surface in TICAM-2 TIR are enclosed by red and yellow dotted lines, respectively.

Yeast two-hybrid analyses showed that TICAM-2 mutants bearing E87A/D88A/D89A and E197A/E198A could not grow completely on SD-LWHA medium due to disruption of their interaction with wild-type TICAM-1 (Fig. 3*C*), suggesting that the acidic cluster consisting of residues Glu87/Asp88/Asp89 in the AA-loop and Glu197/Glu198 in the EE-loop of the TICAM-2 TIR domain might be responsible for association with the TICAM-1 TIR domain (Fig. 3*D*, in magenta). However, in yeast two-hybrid experiments, it is generally difficult to distinguish mutations that disrupt the protein interaction surface from those that disrupt the tertiary structure. To discriminate these two scenarios, the mutant proteins were expressed and subjected to gel-filtration chromatography. We showed the results in *SI Text* and Fig. S3.

Coupled Mutations Identify Additional Binding Sites. Because dimer formation of the TICAM-2 TIR domain is indispensable for interaction with the TICAM-1 TIR domain, we used TICAM-2 TIR domain mutants that harbored no BB-loop mutations in the following yeast two-hybrid experiments. Because the β-strands formed a core structure surrounded by α-helices and loop regions, the residues in the β-strands would be expected to stabilize the structure of the TIR domain. Thus, we applied mutations to the exposed surface residues located on α-helices or loops, based on the NMR structure of TICAM-2 C117H (Fig. S4) and studied further interaction sites between the TICAM-2 and TICAM-1 TIR domains using yeast two-hybrid experiments. The heterotypic interaction between the TICAM-2 wild type and the TICAM-1 mutants was studied using an SD-LWH medium where the 3AT concentration is successively increased (Fig. 4*A*). Tables S2 and S3 list the results of the yeast two-hybrid experiments. Only TICAM-2 mutants involving residues on the CC'-loop between the αC and the αC' helices showed reduced affinity for TICAM-1 as is summarized in Fig. 4*A*. First, the interaction of the F153A/Y154S, Y154S/T155A, and T155A/S156A mutants of the TICAM-2 TIR domain was studied with the wild type of the TICAM-2 TIR domain, showing that these mutants retain the homotypic interaction with the TICAM-2 wild type (Fig. 4*A*, right lane). Next, these mutants were applied to the yeast two-hybrid analyses to study heterotypic interactions with wild-type TICAM-1 and TICAM-1 P434H. Considering that monomeric TICAM-1 P434H can interact with the TICAM-2 dimer, the contact residues should be located near the RK site. Thus, we selected Gln518 and Ile519 on the EE-loop and αE-helix as further candidates for interaction with the TICAM-2 TIR domain.

Among the TICAM-2 TIR domain mutants F153A/Y154S, Y154S/T155A, and T155A/S156A, only the T155A/S156A mutant on the CC'-loop showed reduced interaction with wild type, P434H, and P434H/Q518A/I519A TICAM-1 mutants in a 3AT dose-dependent manner, with higher growth inhibition for the P434H/Q518A/I519A mutant. This result implied that Thr155 and Ser156 in TICAM-2 (designated the "TS site") and Gln518 and

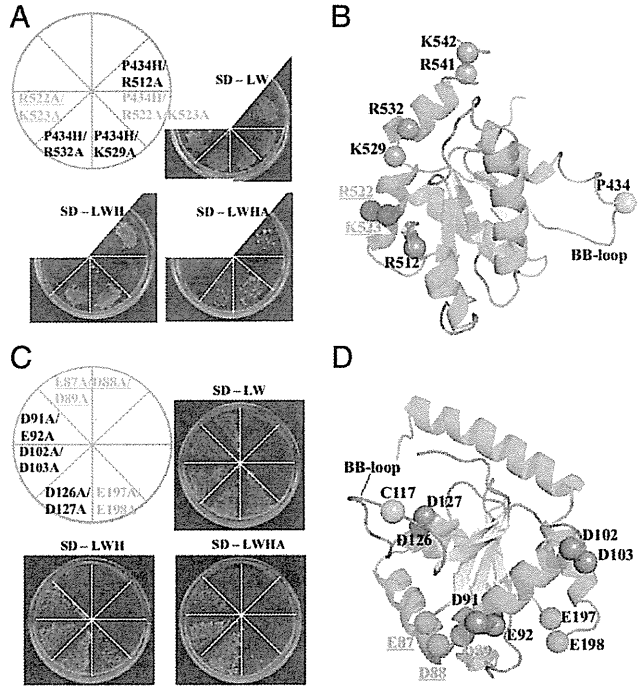

Fig. 3. Heterotypic interaction between TICAM-1 and TICAM-2 TIRs revealed by yeast two-hybrid assays (1). (*A*) Yeast two-hybrid assays using the wild type of the TICAM-2 TIR domain as bait and the mutants of the TICAM-1 TIR domain as prey. (*B*) The basic residues on the EE-loop and αE- and αE'-helices in the TICAM-1 TIR domain (shown as spheres) are mutated to Ala. The residues that disrupt the heterotypic interaction are displayed in cyan. The position of the BB-loop mutation in TICAM-1 TIR is shown in orange. (*C*) Yeast two-hybrid assays using the wild type of the TICAM-1 TIR domain as bait and the mutants of the TICAM-2 TIR domain harboring no BB-loop mutation as prey. (*D*) The acidic residues in the TICAM-2 TIR domain (shown as spheres) are mutated to Ala. The residues that disrupt the heterotypic interaction are displayed in magenta. The position of the BB-loop mutation in TICAM-2 TIR is shown in orange.

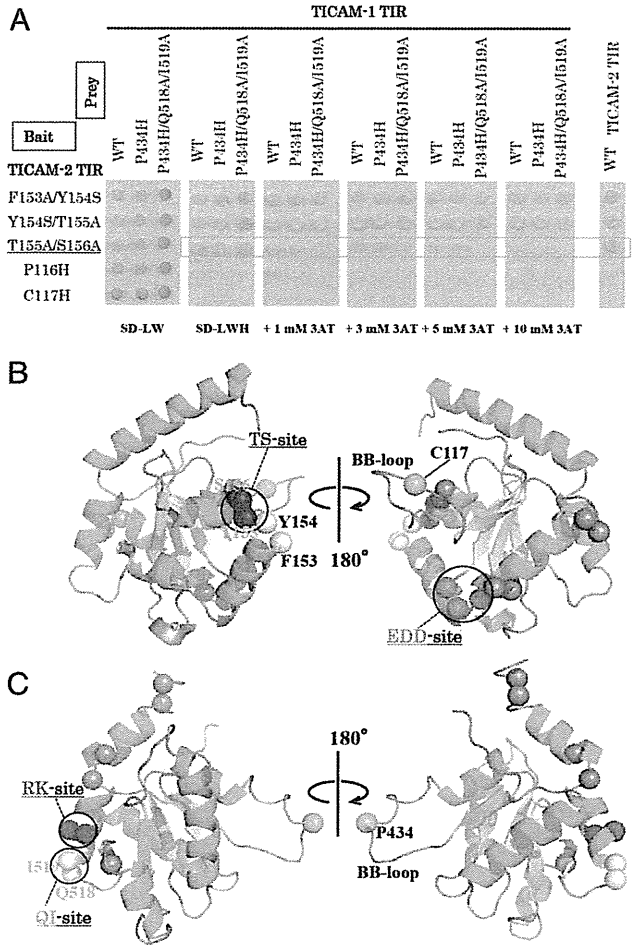

Fig. 4. Heterotypic interaction between TICAM-2 and TICAM-1 TIRs revealed by yeast two-hybrid assays (2). (*A*) Yeast two-hybrid assays using the mutants of TICAM-2 TIR as bait and the wild type and mutants of TICAM-1 TIR as prey. The wild-type TICAM-2 TIR is also used as prey as shown in *Right*. Yeast growth was analyzed with SD-LWH medium supplemented with 3-AT. (*B*) Residue mapping on the structure of TICAM-2 TIR. Thr155 and Ser156 are shown in blue (TS site), and Phe153 and Y154 are shown in white. Acidic residues, Glu87, Asp88, and Asp89 (EDD site), which are critical for interaction with TICAM-1, are shown in magenta. The residue C117 substituted by His is shown in orange. (*C*) Residue mapping on the structure of TICAM-1 TIR. Arg522 and Lys523 (RK site) are shown in cyan, and Gln518 and Ile519 (QI site) are shown in white. The Pro434 substituted by His in BB-loop of TICAM-1 is shown in orange.

Ile519 in TICAM-1 (designated the "QI site") are also involved in the heterotypic interaction (Fig. 4*A*). Intriguingly, the TS site in blue and the EDD site in magenta are located on opposite sides of the TICAM-2 TIR domain (Fig. 4*B*). In TICAM-1, the interacting residues with the TICAM-2 TIR domain are located on the RK site (in cyan) and QI site (in white), which form a wedge-like shape on the TICAM-1 TIR domain surface (Fig. 4*C*).

Restrained Docking of Trimeric TICAM-2/TICAM-1 Complex. The solution structures of the TICAM-1 P434H and TICAM-2 C117H mutants, along with the results of the mutagenesis and yeast two-hybrid assays, permitted docking of the complex formed by two TICAM-2 TIR domains and a single TICAM-1 TIR domain (*SI Text*, Fig. S5).

As shown in Fig. 5, the heterotypic interaction sites on TICAM-2 in the top-ranked model involve the acidic surface of the EDD site on the first TICAM-2 chain and the TS site on the second TICAM-2 chain, located on the opposite side (Fig. 5*A*). Significantly, the TICAM-2 homo-dimer positions the EDD and TS sites next to each other (Fig. 5*A*), forming a concave surface that can accommodate the TICAM-1 TIR domain. The interaction site on TICAM-1 includes the RK site on the αE-helix and the QI site on the EE-loop, which are located on the top of the wedge (Fig. 5*A*). In the top-scoring model, all 7 mutations that abrogated TICAM-2/TICAM-1 binding and 30 out of the 31 mutations that did not affect TICAM-2/TICAM-1 binding were recapitulated in the binding energy calculations (Table S4). The TICAM-2 dimer is symmetrically related by a twofold axis along the BB-loop and is maintained by the BB-loop and αC-helix interactions, respectively, consistent with the TLR10 dimer structure (Fig. 5*B*).

The top view of the interaction surface between the TICAM-2 dimer and the TICAM-1 monomer is shown in Fig. 5*C*, where the binding surface of TICAM-2 is represented by the electrostatic surface potential and TICAM-1 by a ribbon model. As shown in the figure, the RK site interacts with the acidic surface of the EDD site, and the QI site with the TS site (Fig. 5*C*).

Reporter Gene and Binding Assays Using Full-Length TICAM-1 and TICAM-2 Mutants. Based on the yeast two-hybrid analysis, we constructed mammalian expression vectors coding the wild type and various mutants of TICAM-2 and TICAM-1 and measured their IFN-β promoter activation abilities by reporter gene assays. Forcedly expressed wild type TICAM-2 activated the IFN-β promoter in HEK293FT cells in a dose-dependent manner (Fig. 6*A*). In contrast, the TICAM-2 EDD-site mutant E87A/D88A/D89A failed to activate the IFN-β promoter (Fig. 6*A*). Overexpressed TICAM-2 undergoes homo-dimerization, which in turn recruits TICAM-1, resulting in activation of the IFN-β promoter. Therefore, we next analyzed TICAM-2–TICAM-1-dependent IFN-β promoter activation in the presence of limiting amounts of TICAM-1. A marked enhancement of TICAM-1-mediated IFN-β promoter activation was observed with wild-type TICAM-2, and to a lesser extent with the EDD-site TICAM-2 mutant (Fig. 6*B*). In the case of TICAM-1, the RK-site mutant (R522A/K523A) only weakly activated the IFN-β promoter (Fig. 6*C*), consistent with the predicted electrostatic interaction between the acidic surface of the TICAM-2 TIR domain and the basic surface of TICAM-1 observed in the yeast two-hybrid experiments and the docking model. We also measured the NF-κB activation abilities of the EDD-site mutant of TICAM-2 (Fig. S6). Both IFN-β and NF-κB promoter assays demonstrated that the TICAM-2 EDD-site mutant suppressed both signals.

To confirm that the TICAM-2 EDD site is involved in the binding of TICAM-1 TIR domain, a coimmunoprecipitation assay was performed in HEK293FT cells. Although the expression level of TICAM-1, the TICAM-2 wild type, and the TICAM-2 EDD mutant in HEK293FT cells was similar (Fig. S7, *Lower*), the affinity between the TICAM-2 mutant and TICAM-1 was much reduced compared with that between the TICAM-2 wild type and TICAM-1 (Fig. S7, *Upper*). All of the data suggest that the reduced IFN-β promoter activity of the TICAM-2 EDD mutant was due to its reduced affinity to TICAM-1.

Discussion

The oligomerization properties of TIR domains are closely related to their biological functions. This study presents challenges for structural analysis by NMR. Here, we applied dominant-negative BB-loop mutations to the TICAM-1 and TICAM-2 TIR domains that disrupted the oligomerization. To study the interaction between TICAM-1 and TICAM-2 TIR domains, we used yeast two-hybrid experiments in combination with monomeric structural information. Although the yeast two-hybrid method can produce false positives, we could eliminate such false positives by structural analysis of the BB-loop mutants together with gel-filtration studies of the expressed proteins. Using this approach, we identified two binding regions, the EDD site and the TS site, located on the opposite sides of TICAM-2. Our docking calculations, based on yeast two-hybrid data, revealed a TICAM-2 TIR homo-dimer that assumed a twofold axis of

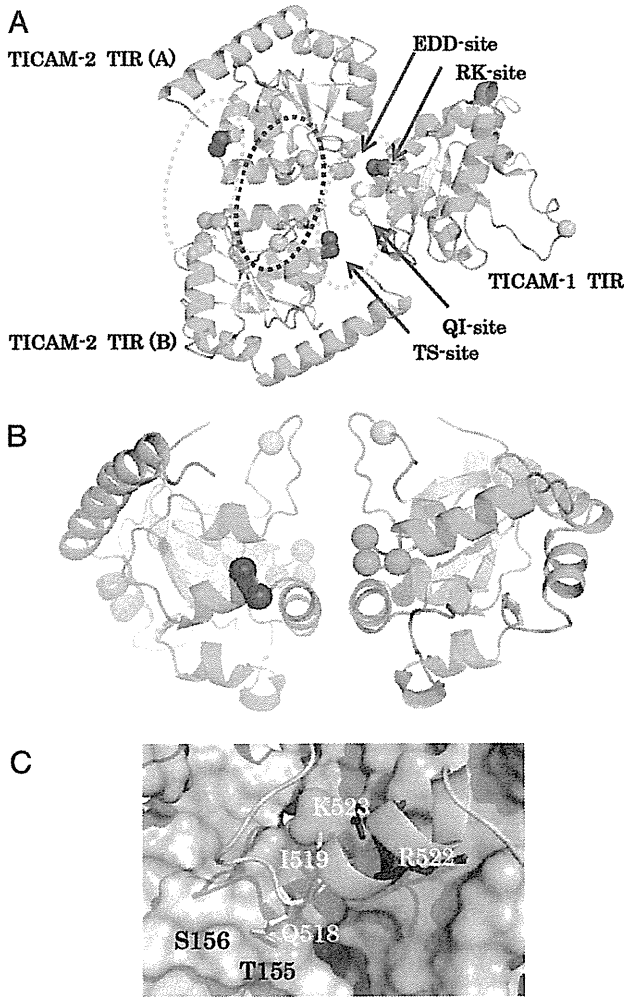

Fig. 5. Docking model of the TIR domains of TICAM-2 and TICAM-1. (*A*) The docking structure comprised of TICAM-2 dimer and TICAM-1 monomer. Homotypic and heterotypic interfaces are enclosed by blue and orange dotted lines, respectively. (*B*) TICAM-2 dimer presenting the binding surface with TICAM-1 TIR. The EDD and TS sites are located at the front surface (also at the back surface) that interact with the wedge of the TICAM-1 TIR (the RK and QI sites). (*C*) The front view of the interacting surface of TICAM-2 is shown in electrostatic surface potential presentation whereas the wedge of the TICAM-1 is presented in ribbon model. The residues on the RK and QI sites are shown in wire model and labeled.

symmetry around the BB-loop, similar to the TLR10 TIR domain structure. Importantly, the two binding regions revealed by the yeast two-hybrid experiments are spatially close in this TICAM-2 homo-dimer structure (Fig. 5*A*). Heterotypic interaction sites on the TICAM-1 TIR domain could also be elucidated by our approach, which indicated that the RK and QI sites are responsible for interaction with TICAM-2. It is notable that this heterotypic interaction does not require dimer formation of the TICAM-1 TIR domain. In our restraint-driven docked model, the wedge-shaped surface containing the RK and QI sites binds to the concave surface formed by the EDD and TS sites belonging to different TICAM-2 TIR domains (Fig. 5 *A* and *B*).

An important conclusion derived from the present study is that the homo-dimerization of the TICAM-2 TIR domains presents a surface that recruits the monomeric moiety of the TICAM-1 TIR domain. In our previous reports, we showed that TLR4 binds the TICAM-2 wild type, but the interaction is disrupted by the BB-loop mutation of TLR4, whereas the BB-loop mutant of TICAM-2 still binds to TLR4 wild type based on the yeast two-hybrid experiments (1). We also showed that the TICAM-1 BB-loop mutant still interacts with the TIR domain of TLR3 wild type (27). Taken together, these results suggest a unique paradigm in which dimer formation of the upstream TIR domain is essential for recruitment of the monomeric moiety of the downstream TIR dimer. Consistent with this paradigm, BB-loop mutants of TLR3 and TLR4 as well as TICAM-1 and TICAM-2 completely abrogate downstream signaling.

It is notable that the myristoylation of TICAM-2 at the N terminus is essential for its localization on the plasma membrane or endosome, and colocalization with TLR4 (32). Interestingly, according to the present TICAM-2 TIR dimer model, the N termini of both TICAM-2 TIR domains are oriented in the same direction, permitting anchoring of the TICAM-2 dimer to the membrane.

A current consensus is that LPS on the surface of Gram-negative bacteria induces clustering of TLR4, leading to formation of the active TLR4 TIR dimer, which triggers activation of the MyD88 and TICAM-1 pathways. Recently, the structure of the Myddosome, a molecular complex mediated by the death domains of MyD88, IRAK4, and IRAK1/2, was determined (33–35). This TICAM-1/2 structural study, on the other hand, would allow us to speculate a model that the TLR4 TIR dimer bridges the TICAM-2 TIR dimer, which further couples with the TICAM-1 TIR, generating an extended signaling network downstream of TLR4. The present work proposes a key for future analysis about an IFN-inducing signaling complex in the context of TLR4-mediated LPS signaling. Recent studies showed the importance of lateral TLR3 clustering mediated by TICAM-1 for downstream signaling (36), consistent with our model.

Our reconstitution study revealed that the TICAM1/2 heterodimer formation is reproducible in HEK293FT cells and that TICAM-2 EDD mutant has less ability to recruit TICAM-1 than wild type (Fig. S7). Reporter activity reflecting IFN induction is accordingly decreased (Fig. 6). Thus, the proposed model is at least right in the formation of the two-adaptor complex. However, herein we only abstracted the complex of TICAM-1 and TICAM-2 from the IFN-inducing axis of LPS signaling of TLR4, which consists of an array of many different molecules. Reconstituting the optimal LPS–IFN signal axis in human TICAM-2 knockout cells will be required to test physiological importance of the TICAM-2 EDD domain.

Materials and Methods

For details, see *SI Materials and Methods*.

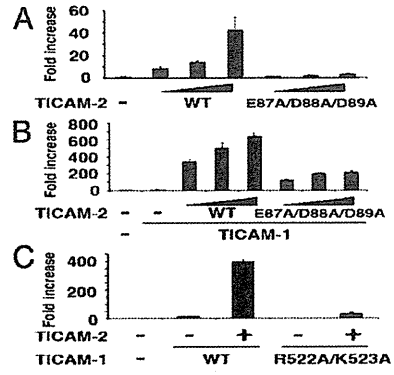

Fig. 6. Functional assays of TICAM-1 and TICAM-2 mutants in mammalian cells. (*A*) TICAM-2–dependent IFN-β promoter activation. IFN-β promoter activity was reduced by the E87A/D88A/D89A mutation in TICAM-2. (*B*) TICAM-2-TICAM-1–dependent IFN-β promoter activation. IFN-β promoter activity was reduced by the E87A/D88A/D89A mutation in TICAM-2. (*C*) TICAM-2-TICAM-1–dependent IFN-β promoter activation. The mutation of R522/K523 in TICAM-1 reduced IFN-β promoter activation.

Protein Expression and Purification. The human TICAM-1 gene encoding the TIR domain (387–545) with mutation of Pro434 to His was cloned into the pET22b (Novagen) vector. The human TICAM-2 gene encoding the TIR domain (75–235) with mutation of Cys117 to His was cloned into the pGEX6p-1 (GE healthcare) vector.

NMR Measurements and Structure Calculation. NMR data for chemical shift assignments for TICAM-1 P434H and TICAM-2 C117H were collected using a suite of triple resonance experiments on Varian UNITY INOVA 600 and 800 spectrometers.

Yeast Two-Hybrid Analysis. The TIR domains were constructed by direct cloning of two-step PCR products using mutant oligonucleotide primers and subcloned into pGBKT7 and pGADT7 plasmid (Clontech).

Restrained Docking Calculations. Two docking calculations were made to generate representative TICAM-2 TIR homo-dimer models, from which trimeric TICAM-2/TICAM-1 models were then constructed.

Luciferase Reporter Gene Assay. Mutants of TICAM-1(1–566) and TICAM-2(1–235) were generated using PCR and subcloned into pEF-BOS vector.

Immunoprecipitation and Immunoblot Analysis. FLAG-tagged TICAM-2 were immunoprecipitated using anti-FLAG mAb (2.5 μg per sample) and Protein G Sepharose (GE healthcare).

ACKNOWLEDGMENTS. This research is supported by the Japan Society for the Promotion of Science through its "Funding Program for World-Leading Innovative R&D on Science and Technology."

1. Oshiumi H, et al. (2003) TIR-containing adapter molecule (TICAM)-2, a bridging adapter recruiting to toll-like receptor 4 TICAM-1 that induces interferon-beta. *J Biol Chem* 278(50):49751–49762.
2. Oshiumi H, Matsumoto M, Funami K, Akazawa T, Seya T (2003) TICAM-1, an adaptor molecule that participates in Toll-like receptor 3-mediated interferon-beta induction. *Nat Immunol* 4(2):161–167.
3. Yamamoto M, et al. (2003) TRAM is specifically involved in the Toll-like receptor 4-mediated MyD88-independent signaling pathway. *Nat Immunol* 4(11):1144–1150.
4. Takeuchi O, Akira S (2010) Pattern recognition receptors and inflammation. *Cell* 140(6):805–820.
5. Yamamoto M, Takeda K, Akira S (2004) TIR domain-containing adaptors define the specificity of TLR signaling. *Mol Immunol* 40(12):861–868.
6. Gay NJ, Gangloff M, Weber AN (2006) Toll-like receptors as molecular switches. *Nat Rev Immunol* 6(9):693–698.
7. Gay NJ, Gangloff M (2007) Structure and function of Toll receptors and their ligands. *Annu Rev Biochem* 76:141–165.
8. Fitzgerald KA, et al. (2003) LPS-TLR4 signaling to IRF-3/7 and NF-kappaB involves the toll adapters TRAM and TRIF. *J Exp Med* 198(7):1043–1055.
9. Xu Y, et al. (2000) Structural basis for signal transduction by the Toll/interleukin-1 receptor domains. *Nature* 408(6808):111–115.
10. Tao X, Xu Y, Zheng Y, Beg AA, Tong L (2002) An extensively associated dimer in the structure of the C713S mutant of the TIR domain of human TLR2. *Biochem Biophys Res Commun* 299(2):216–221.
11. Khan JA, Brint EK, O'Neill LA, Tong L (2004) Crystal structure of the Toll/interleukin-1 receptor domain of human IL-1RAPL. *J Biol Chem* 279(30):31664–31670.
12. Ohnishi H, et al. (2009) Structural basis for the multiple interactions of the MyD88 TIR domain in TLR4 signaling. *Proc Natl Acad Sci USA* 106(25):10260–10265.
13. Valkov E, et al. (2011) Crystal structure of Toll-like receptor adaptor MAL/TIRAP reveals the molecular basis for signal transduction and disease protection. *Proc Natl Acad Sci USA* 108(36):14879–14884.
14. Lin Z, Lu J, Zhou W, Shen Y (2012) Structural insights into TIR domain specificity of the bridging adaptor Mal in TLR4 signaling. *PLoS ONE* 7(4):e34202.
15. Chan SL, Mukasa T, Santelli E, Low LY, Pascual J (2010) The crystal structure of a TIR domain from Arabidopsis thaliana reveals a conserved helical region unique to plants. *Protein Sci* 19(1):155–161.
16. Bernoux M, et al. (2011) Structural and functional analysis of a plant resistance protein TIR domain reveals interfaces for self-association, signaling, and autoregulation. *Cell Host Microbe* 9(3):200–211.
17. Chan SL, et al. (2009) Molecular mimicry in innate immunity: Crystal structure of a bacterial TIR domain. *J Biol Chem* 284(32):21386–21392.
18. Nyman T, et al. (2008) The crystal structure of the human toll-like receptor 10 cytoplasmic domain reveals a putative signaling dimer. *J Biol Chem* 283(18):11861–11865.
19. Poltorak A, et al. (1998) Defective LPS signaling in C3H/HeJ and C57BL/10ScCr mice: Mutations in Tlr4 gene. *Science* 282(5396):2085–2088.
20. Gautam JK, Ashish, Comeau LD, Krueger JK, Smith MF, Jr. (2006) Structural and functional evidence for the role of the TLR2 DD loop in TLR1/TLR2 heterodimerization and signaling. *J Biol Chem* 281(40):30132–30142.
21. Dunne A, Ejdeback M, Ludidi PL, O'Neill LA, Gay NJ (2003) Structural complementarity of Toll/interleukin-1 receptor domains in Toll-like receptors and the adaptors Mal and MyD88. *J Biol Chem* 278(42):41443–41451.
22. Li C, Zienkiewicz J, Hawiger J (2005) Interactive sites in the MyD88 Toll/interleukin (IL) 1 receptor domain responsible for coupling to the IL1β signaling pathway. *J Biol Chem* 280(28):26152–26159.
23. Radons J, et al. (2003) The interleukin 1 (IL-1) receptor accessory protein TolI/IL-1 receptor domain: analysis of putative interaction sites in vitro mutagenesis and molecular modeling. *J Biol Chem* 278(49):49145–49153.
24. Bovijn C, et al. (2012) Identification of interaction sites for dimerization and adapter recruitment in Toll/interleukin-1 receptor (TIR) domain of Toll-like receptor 4. *J Biol Chem* 287(6):4088–4098.
25. Núñez Miguel R, et al. (2007) A dimer of the Toll-like receptor 4 cytoplasmic domain provides a specific scaffold for the recruitment of signalling adaptor proteins. *PLoS ONE* 2(8):e788.
26. Seya T, Oshiumi H, Sasai M, Akazawa T, Matsumoto M (2005) TICAM-1 and TICAM-2: Toll-like receptor adapters that participate in induction of type 1 interferons. *Int J Biochem Cell Biol* 37(3):524–529.
27. Funami K, Sasai M, Oshiumi H, Seya T, Matsumoto M (2008) Homo-oligomerization is essential for Toll/interleukin-1 receptor domain-containing adaptor molecule-1-mediated NF-kappaB and interferon regulatory factor-3 activation. *J Biol Chem* 283(26):18283–18291.
28. Holm L, Park J (2000) DaliLite workbench for protein structure comparison. *Bioinformatics* 16(6):566–567.
29. Kawabata T (2003) MATRAS: A program for protein 3D structure comparison. *Nucleic Acids Res* 31(13):3367–3369.
30. Kawabata T, Nishikawa K (2000) Protein structure comparison using the markov transition model of evolution. *Proteins* 41(1):108–122.
31. Chien CT, Bartel PL, Sternglanz R, Fields S (1991) The two-hybrid system: A method to identify and clone genes for proteins that interact with a protein of interest. *Proc Natl Acad Sci USA* 88(21):9578–9582.
32. Rowe DC, et al. (2006) The myristoylation of TRIF-related adaptor molecule is essential for Toll-like receptor 4 signal transduction. *Proc Natl Acad Sci USA* 103(16):6299–6304.
33. Lin SC, Lo YC, Wu H (2010) Helical assembly in the MyD88-IRAK4-IRAK2 complex in TLR/IL-1R signalling. *Nature* 465(7300):885–890.
34. Gay NJ, Gangloff M, O'Neill LA (2011) What the Myddosome structure tells us about the initiation of innate immunity. *Trends Immunol* 32(3):104–109.
35. Kersse K, Verspurten J, Vanden Berghe T, Vandenabeele P (2011) The death-fold superfamily of homotypic interaction motifs. *Trends Biochem Sci* 36(10):541–552.
36. Luo J, et al. (2012) Lateral clustering of TLR3:dsRNA signaling units revealed by TLR3ecd:3Fabs quaternary structure. *J Mol Biol* 421(1):112–124.

The MyD88 Pathway in Plasmacytoid and CD4$^+$ Dendritic Cells Primarily Triggers Type I IFN Production against Measles Virus in a Mouse Infection Model

Hiromi Takaki,* Makoto Takeda,† Maino Tahara,† Masashi Shingai,*,[1] Hiroyuki Oshiumi,* Misako Matsumoto,* and Tsukasa Seya*

Infection by measles virus (MV) induces type I IFN via the retinoic acid–inducible gene I/melanoma differentiation–associated gene 5/mitochondrial antiviral signaling protein (MAVS) pathway in human cells. However, the in vivo role of the MAVS pathway in host defense against MV infection remains undetermined. CD150 transgenic (Tg) mice, which express human CD150, an entry receptor for MV, with the disrupting IFNR gene (*Ifnar*$^{-/-}$), are susceptible to MV and serve as a model for MV infection. In this study, we generated CD150Tg/*Mavs*$^{-/-}$ mice and examined MV permissiveness compared with that in CD150Tg/*Ifnar*$^{-/-}$ mice. MV replicated mostly in the spleen of i.p.-infected CD150Tg/*Ifnar*$^{-/-}$ mice. Strikingly, CD150Tg/*Mavs*$^{-/-}$ mice were not permissive to MV in vivo because of substantial type I IFN induction. MV barely replicated in any other organs tested. When T cells, B cells, and dendritic cells (DCs) isolated from CD150Tg/*Mavs*$^{-/-}$ splenocytes were cultured with MV in vitro, only the DCs produced type I IFN. In vitro infection analysis using CD150Tg/*Mavs*$^{-/-}$ DC subsets revealed that CD4$^+$ and plasmacytoid DCs, but not CD8α$^+$ and CD8α$^-$CD4$^-$ double negative DCs, were exclusively involved in type I IFN production in response to MV infection. Because CD150Tg/*Mavs*$^{-/-}$ mice turned permissive to MV by anti-IFNAR Ab, type I IFN produced by CD4$^+$ DCs and plasmacytoid DCs plays a critical role in antiviral protection for neighboring cells expressing IFNAR. Induction of type I IFN in these DC subsets was abolished by the MyD88 inhibitory peptide. Thus, production of type I IFN occurs via the MyD88-dependent and MAVS-independent signaling pathway during MV infection. *The Journal of Immunology*, **2013, 191: 4740–4747.**

Type I IFNs (IFN-α/β) are crucial for protection against viral infections (1). Viral RNA is detected by cytosolic RNA sensors and induces expression of type I IFN (2). Extracellular dsRNA of a virus product is detected by the endosomal TLR3, whereas intracellular dsRNA is sensed by the retinoic acid–inducible gene I (RIG-I) and the melanoma differentiation–associated gene 5 (MDA5) (3). Upon recognizing dsRNA, TLR3 recruits the Toll/IL-1R (TIR) homology domain–containing adaptor molecule 1 (TICAM-1, also referred to as TRIF) and induces type I IFN production (4, 5). The RIG-I–like receptors (RLRs), RIG-I and MDA5, signal via the mitochondrial antiviral signaling protein (MAVS; also known as VISA, Cardif, or IPS-1) and also induce type I IFN expression (6). Knocking out these adaptor molecules results in failure to activate the transcription factors IFN regulatory factor (IRF)-3 and IRF-7, leading to an incompetence in type I IFN production and antiviral host defense (3, 7, 8). Type I IFN induction following the recognition of measles virus (MV) RNA is dependent on the RIG-I/MDA5-MAVS pathway in human epithelial cell lines (9, 10). However, the role of the RIG-I/MDA5-MAVS pathway during in vivo MV infection remains undetermined.

MV, of the genus *Morbillivirus* from the Paramyxoviridae family, is a highly pathogenic, nonsegmented negative single-stranded RNA virus that causes respiratory distress and immunosuppression in humans (11). Wild-type strains of MV enter cells via human CD150, which is also referred to as signaling lymphocyte activation molecule (12), and human poliovirus receptor–like protein 4 (13, 14). Expression of these receptors is restricted either to activated lymphocytes, dendritic cells (DCs), and macrophages for CD150 or to the basolateral surface of epithelial cells for PVRL4 (15). Among these cell populations, CD11c$^+$ DCs and alveolar macrophages (AMs) are reported to be the first target cells of early-phase MV infection in the CD150 transgenic (Tg) mouse model (16, 17) and in nonhuman primates (18, 19). Moreover, DCs are found to be involved in pathogenesis and immunosuppression during and after acute MV infection (20, 21). However, it is unclear how DCs and macrophages recognize MV RNA to produce type I IFN.

Human CD150Tg mice, which are slightly permissive to MV, are used to study host responses against MV infection in vivo (16, 22–24). CD150Tg/*Ifnar*$^{-/-}$ mice, which are generated by crossing CD150Tg mice with *Ifnar*$^{-/-}$ mice, are susceptible to MV infection

*Department of Microbiology and Immunology, Graduate School of Medicine, Hokkaido University, Kita-ku, Sapporo 060-8638, Japan; and †Department of Virology 3, National Institute of Infectious Diseases, Gakuen 4-7-1, Musashimurayama, Tokyo 208-0011, Japan

[1]Current address: Laboratory of Molecular Microbiology, National Institute of Allergy and Infectious Diseases, National Institutes of Health, Bethesda, MD.

Received for publication July 3, 2013. Accepted for publication August 28, 2013.

This work was supported in part by grants-in-aid from the Ministry of Education, Science, and Culture (Specified Project for Advanced Research) and the Ministry of Health, Labor, and Welfare of Japan; the Japan Society for the Promotion of Science Fellows and Support Office for Female Researchers in Hokkaido University; the Takeda Foundation and the Waxmann Foundation; and the Program of Founding Research Centers for Emerging and Reemerging Infectious Diseases, Ministry of Education, Culture, Sports, Science and Technology.

Address correspondence and reprint requests to Prof. Tsukasa Seya and Dr. Hiromi Takaki, Department of Microbiology and Immunology, Hokkaido University Graduate School of Medicine, Kita 15, Nishi 7, Kita-ku, Sapporo 060-8638, Japan. E-mail addresses: seya-tu@pop.med.hokudai.ac.jp (T.S.) and tahiromi@sci.hokudai.ac.jp (H.T.)

The online version of this article contains supplemental material.

Abbreviations used in this article: AM, alveolar macrophage; BMDC, bone marrow–derived DC; cDC, conventional DC; DC, dendritic cell; DN, double negative; IRF, IFN regulatory factor; LN, lymph node; MAVS, mitochondrial antiviral signaling protein; MDA5, melanoma differentiation–associated gene 5; MOI, multiplicity of infection; MV, measles virus; MyD88, myeloid differentiation factor 88; pDC, plasmacytoid DC; PDCA-1, pDC Ag 1; RIG-I, retinoic acid–inducible gene I; RLR, RIG-I–like receptor; Tg, transgenic; TICAM-1, Toll/IL-1R homology domain–containing adaptor molecule 1; TIR, Toll/IL-1R.

www.jimmunol.org/cgi/doi/10.4049/jimmunol.1301744

and serve as a useful mouse model (16, 24). In the current study, using the CD150Tg mouse model in combination with *Mavs*$^{-/-}$, *Irf3*$^{-/-}$/*Irf7*$^{-/-}$, and *Ticam1*$^{-/-}$ mice, we found that CD150Tg/*Mavs*$^{-/-}$ mice were not permissive to MV in vivo, whereas CD150Tg/*Irf3*$^{-/-}$/*Irf7*$^{-/-}$ mice were permissive. Furthermore, CD150Tg/*Mavs*$^{-/-}$ plasmacytoid DCs (pDCs) and CD4$^+$ DCs produced type I IFN in response to MV infection in vitro. Analysis using the myeloid differentiation factor 88 (MyD88) inhibitory peptide and MyD88$^{-/-}$ mice revealed that type I IFN production in these DC subsets was dependent on the MyD88 pathway. To our knowledge, this is the first study to show that type I IFN induction in MV-infected mouse DCs depends on the MyD88 pathway. The properties of the MV-permissive mouse DC subsets may be crucial for ensuring immune response, including immunosuppression during MV infection.

Materials and Methods

Mice

All mice were backcrossed to C57BL/6 mice more than eight times before use. CD150Tg (16), *Ticam1*$^{-/-}$ (25), and *Mavs*$^{-/-}$ (26) mice were generated in our laboratory. *Irf3*$^{-/-}$ and *Irf7*$^{-/-}$ mice were provided by Dr. T. Taniguchi (University of Tokyo, Tokyo, Japan). *Myd88*$^{-/-}$ mice were provided by Drs. K. Takeda and S. Akira (Osaka University, Osaka, Japan). All mice were maintained under specific pathogen–free conditions in the Animal Facility at Hokkaido University Graduate School of Medicine (Sapporo, Japan) and used when they were between 6 and 12 wk of age. This study was carried out in strict accordance with the recommendations in the National Institutes of Health *Guide for the Care and Use of Laboratory Animals*. The protocol was approved by the Committee on the Ethics of Animal Experiments in the Animal Safety Center, Hokkaido University. All mice were used according to the guidelines of the Institutional Animal Care and Use Committee of Hokkaido University, which approved this study as no.13-0024. All inoculation and experimental manipulation were performed with the animals under anesthesia that was induced and maintained with pentobarbital sodium, and all efforts were made to minimize suffering.

Virus and cell culture

Vero/CD150 cells were maintained in DMEM supplemented with 10% heat-inactivated FBS and antibiotics. IC323, corresponding to the IC-B strain of MV (27), was recovered from the plasmid p(+)MV323 encoding the antigenomic IC-B sequence (28). IC323-Luci (MV-luciferase), which expresses the reporter *Renilla* luciferase from the first gene position of the MV genome, was a kind gift from Dr. Y. Yanagi (Kyushu University, Fukuoka, Japan) (29). MV-luciferase was maintained in Vero/CD150 cells (30). Virus titer was determined as PFUs on Vero/CD150, and the multiplicity of infection (MOI) of each experiment was calculated based on this titer (27). Splenic CD19$^+$, CD4$^+$, CD8$^+$ cells, and CD11c$^+$ DCs were isolated using anti-CD19, anti-CD4, anti-CD8, and anti-CD11c MACS beads (Miltenyi Biotec). Splenic CD8α^+ DCs, CD4$^+$ DCs, and double negative (DN) DCs were isolated using CD8α^+ or CD4$^+$ DC isolation kits (Miltenyi Biotec) according to the manufacturer's instructions. For isolation of pDCs and conventional DCs (cDCs), spleens were treated with 400 IU Mandle U/ml collagenase D (Roche) at 37°C for 25 min in HBSS (Sigma-Aldrich). EDTA was added, and the cell suspension was incubated for an additional 5 min at 37°C. After removal of RBCs with ammonium chloride–potassium lysis buffer, CD11c$^+$ DCs were isolated using CD11c MACS beads. MACS-sorted DCs were stained with anti-CD11b–FITC, anti-pDC Ag 1 (PDCA-1)–PE (eBioscience), and anti-CD11c–allophycocyanin (BioLegend) and sorted using a FACSAria II (BD). The purity of sorted cells was > 98%.

FACS analysis

For pDC staining, splenocytes were stained with anti-CD11c–allophycocyanin (BioLegend), anti–PDCA-1–PE (BioLegend), and anti-human CD150–FITC (eBiosciences). For CD4$^+$ DCs, CD8$^+$ DCs, and DN DCs staining, splenocytes were stained with anti-CD11c–allophycocyanin (BioLegend), anti-CD4–PerCP (BioLegend), anti-CD8–PE (BioLegend), and anti-human CD150–FITC. For B cell staining, splenocytes were stained with anti-B220–allophycocyanin (BioLegend), anti-CD19–PE (BioLegend), and anti-human CD150–FITC. For T cell staining, anti-CD3–allophycocyanin (BioLegend), anti-CD4–PerCP, anti-CD8–PE, and anti-human CD150–FITC were used. Fluorescence intensity of CD150 was measured by flow cytometry. For TLR7 intracellular staining in pDCs, DCs were stained with anti-TLR7–FITC (IMGENEX), anti-CD11c–allophycocyanin, and anti–PDCA-1–PE using the BD Cytofix/Cytoperm Kit (BD Biosciences). For TLR7 intracellular staining in CD4$^+$, CD8$^+$, and DN DCs, DCs were stained with anti-TLR7–FITC (IMGENEX), anti-CD11c–allophycocyanin, anti-CD4–PerCP, and anti-CD8–PE, using the BD Cytofix/Cytoperm Kit (BD Biosciences). Stained cells were analyzed by flow cytometry.

Experimental infection and luciferase assay

Mice were infected i.p. with MV-luciferase at the indicated doses. For in vivo blockade of the type I IFNR, mice were i.p. injected with 2.5 mg MAR1-5A3, a mAb against IFNAR-1 (BioLegend), 1 d prior to infection. Tissues were collected from the mice at different time points, and the efficiency of infection was measured by luciferase assay. Cells (1×10^7) from various tissues were harvested in 100 μl lysis buffer. The amount of protein in each lysate was determined by bicinchoninic acid assay. Luciferase assay was performed using a Dual-Luciferase Reporter Assay System (Promega), and luciferase activity was read using a Lumat LB 9507 (Berthold Technologies). To measure the efficiency of in vitro infection, cells (5×10^4–4×10^5) were harvested in 25 μl lysis buffer for luciferase assay. For MyD88 inhibition assay, cells were pretreated with 50 μM MyD88 inhibitory peptide (RQIKIWFQNRRMKWKK-RDVLPGTCVNS-NH2; InvivoGen) or the control peptide (RQIKIWFQNRRMKWKK-SLHGRGDPMEAFII-NH2; InvivoGen) for 6 h, and then cells were infected with MV. MyD88 inhibitory peptide contains a sequence from the MyD88 TIR homodimerization domain (RDVLPGT) preceded with a protein transduction sequence (RQIKIWFQNRRMKWKK) derived from antennapedia, which enables the peptide to translocate through the cell membrane. For intratracheal infection with MV, mice were anesthetized and injected with MV-luciferase (8×10^5 PFU/50 μl in PBS) intratracheally. At 3 d after inoculation, mice were sacrificed and perfused with PBS containing 10 mM EDTA from the right ventricle. Lung lobes were isolated, and collagenase buffer [150 U/ml collagenase D (Roche), 10 μg/ml DNase I (Takara), and 5% FCS in RPMI 1640 medium] was injected into the lobes, using a 27-gauge needle. The lobes were then shredded into small pieces and incubated at 37°C for 45 min. During the last 5 min, EDTA was added at 10 mM. Any remaining small pieces were dispersed by passage in and out through a 20-gauge needle, and the suspension was passed through nylon mesh to remove debris. A single-cell suspension was prepared after RBC lysis. A total of 2×10^6 cells were harvested in 100 μl lysis buffer for luciferase assay.

ELISA

Culture supernatants of cells ($1–5 \times 10^5$) seeded on 96-well plates were collected and analyzed for cytokine levels, using ELISA. ELISA kits for mouse IFN-α and IFN-β were from PBL Biomedical Laboratories. Assays were performed according to the manufacturer's instructions.

RT-PCR and real-time PCR

Total RNA was prepared using TRIzol Reagent (Invitrogen) following the manufacturer's instructions. RT-PCR was carried out using a High Capacity cDNA Reverse Transcription Kit (Applied Biosystems) according to the manufacturer's instructions. Real-time PCR was performed using a StepOne Real-Time PCR System (Applied Biosystems). The following oligonucleotides were used for *β-actin*: 5′-TTTGCAGCTCCTTCGTTGC-3′ and 5′-TCGTCATCCATGGCGAACT-3′; for *Ifn-β*: 5′-CCAGCTCCAAGAAAGGACGA-3′ and 5′-CGCCCTGTAGGTGAGGTTGAT-3′; for *Ifn-α4*: 5′-CTGCTGGCTGTGAGGACATACT-3′ and 5′-AGGCACAGAGGCTGTGTTTCTT-3′; for *Ifit1*: 5′-TGTGCTGAGATGGACTGTGAG-3′ and 5′-TTTCTGGCTCCACTTTCAGAG-3′; for *Cxcl10*: 5′-GTGTTGAGATCATTGCCACGA-3′ and 5′-GCGTGGCTTCACTCCAGTTAA-3′; for *Tlr7*: 5′-GTATGCCGCCAAATCTAAAG-3′ and 5′-GGCTGAGGTCCAAAATTTCC-3′; and for *MV-P*: 5′-cTGCATCACGCAGTGTAATC-3′ and 5′-CTGGTGGAACTTGGCAAGATC-3′. Levels of target mRNAs were normalized to *β-actin*, and fold-induction of transcripts was calculated using the ddCT method relative to unstimulated cells.

Statistical analyses

Statistical significance of differences between groups was determined by the Student *t* test using Microsoft Excel software. The *p* values < 0.05 were considered significant.

Results

CD150Tg/Mavs$^{-/-}$ *mice are not permissive to MV*

To quantitate the efficiency of MV infection, we used a recombinant MV-luciferase that expresses the reporter *Renilla* luciferase from the insert of the MV genome (29). CD150 expression levels did

not differ among various spleen cells from CD150Tg, CD150Tg/*Ifnar*$^{-/-}$, CD150Tg/*Irf3*$^{-/-}$/*Irf7*$^{-/-}$, CD150Tg/*Ticam1*$^{-/-}$ or CD150Tg/*Mavs*$^{-/-}$ mice (Supplemental Fig. 1). Each knockout mouse strain was i.p. injected with 1×10^6 PFU of MV-luciferase. In accord with previous data (16, 22), luciferase activity in various tissues derived from MV-infected CD150Tg mice was very low 2 d after inoculation (Fig. 1A). In contrast, luciferase activity was predominantly increased in spleen and lymph nodes (LNs) derived from MV-infected CD150Tg/*Ifnar*$^{-/-}$ mice, compared with other tissues (Fig. 1A). *MV-P* mRNA expression was also increased in MV-infected CD150Tg/*Ifnar*$^{-/-}$ spleen and LNs, similarly to luciferase activity (Fig. 1B). These results indicate that spleen and LNs are the major target tissues of i.p.-injected MV in CD150Tg/*Ifnar*$^{-/-}$ mice, as shown in a previous report (24). Luciferase activity was increased in the lung of CD150Tg/*Ifnar*$^{-/-}$, but not CD150Tg/*Mavs*$^{-/-}$, mice after intratracheal injection of MV

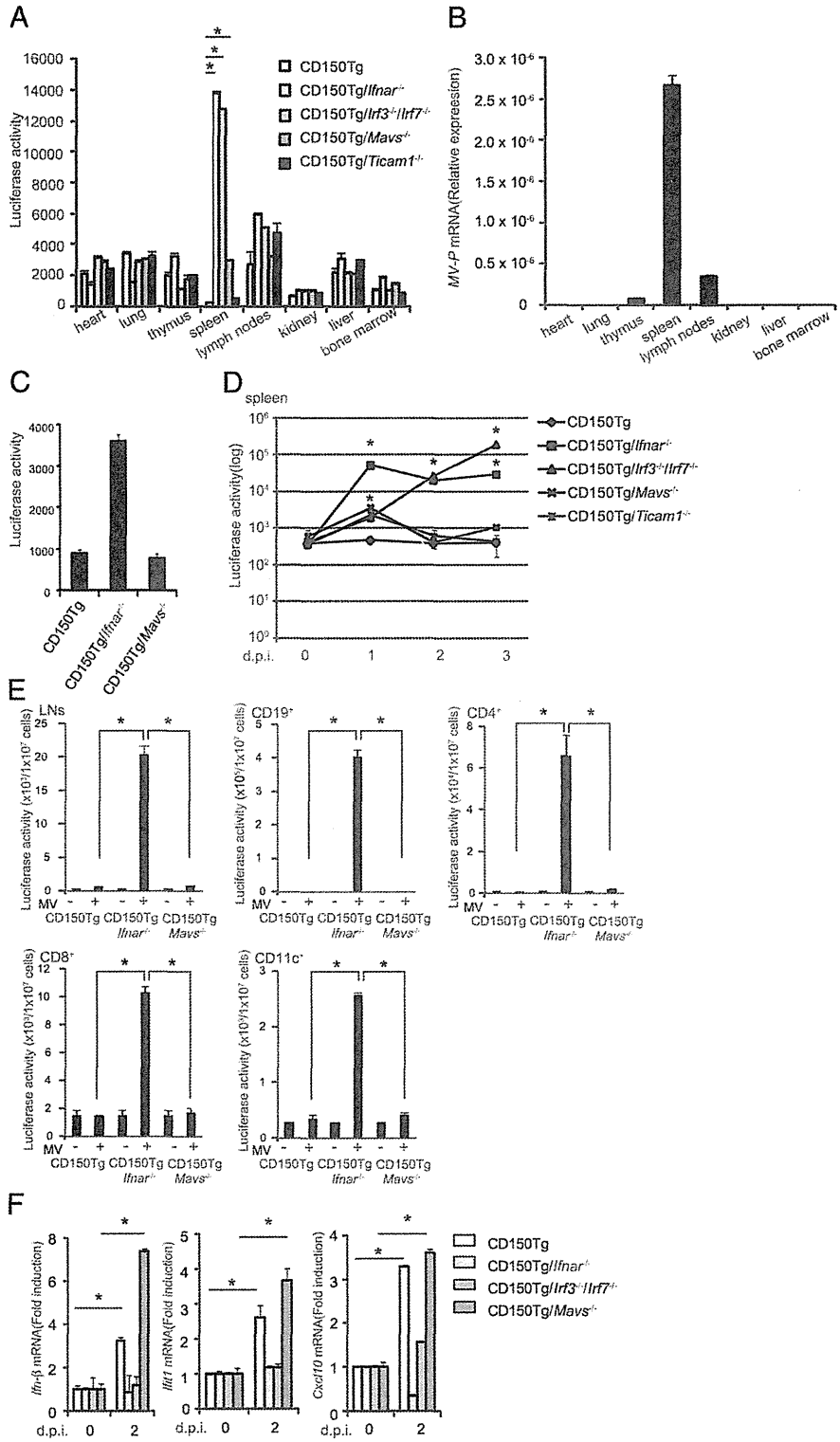

FIGURE 1. CD150Tg/*Mavs*$^{-/-}$ mice were resistant to in vivo MV infection. (**A**) CD150Tg, CD150Tg/*Ifnar*$^{-/-}$, CD150Tg/*Irf3*$^{-/-}$/*Irf7*$^{-/-}$, CD150Tg/*Mavs*$^{-/-}$, and CD150Tg/*Ticam1*$^{-/-}$ mice were infected i.p. with 1×10^6 PFU MV-luciferase. After 2 d, cells were isolated from each organ and lysed with lysis buffer for luciferase assay. The amount of protein in each lysate was determined by bicinchoninic acid assay. Luciferase activity in each lysate was measured and normalized by the amount of protein. Data are shown as luciferase activity per 1 mg of protein and means ± SD of three independent samples. *$p < 0.05$. (**B**) CD150Tg/*Ifnar*$^{-/-}$ mice were infected with MV (1×10^6 PFU). At 2 d after inoculation, total RNA was collected from the indicated tissues, and the expression level of *MV-P* mRNA in each tissue was determined by real-time PCR. *MV-P* mRNA expression is shown as expression relative to *β-actin*. Data are means ± SD of three independent samples. (**C**) CD150Tg, CD150Tg/*Ifnar*$^{-/-}$, and CD150Tg/*Mavs*$^{-/-}$ mice were intratracheally injected with MV-luciferase (8×10^5 PFU). At 3 d after inoculation, luciferase activity was measured in cells from lungs. Data are means ± SD of two independent samples. (**D**) At the indicated days post infection (d.p.i.), luciferase activity in 1×10^7 splenocytes was measured. Three mice were analyzed for each genotype. Data are representative of two independent experiments. *$p < 0.05$ versus CD150Tg. (**E**) CD150Tg, CD150Tg/*Ifnar*$^{-/-}$, and CD150Tg/*Mavs*$^{-/-}$ mice were infected i.p. with 1×10^6 PFU MV-luciferase. At 2 d.p.i., CD19$^+$, CD4$^+$, CD8$^+$, and CD11c$^+$ cells were isolated from splenocytes, using anti-CD19, anti-CD4, anti-CD8, and anti-CD11c MACS beads. Luciferase activity in CD19$^+$, CD4$^+$, CD8$^+$, and CD11c$^+$ cells, as well as LNs, was measured and normalized by the total number of cells. Data are shown as the luciferase activity per 1×10^7 cells. Data are means ± SD of three independent samples. *$p < 0.05$. (**F**) CD150Tg, CD150Tg/*Ifnar*$^{-/-}$, CD150Tg/*Irf3*$^{-/-}$/*Irf7*$^{-/-}$, and CD150Tg/*Mavs*$^{-/-}$ mice were infected i.p. with 1×10^6 PFU MV-luciferase. At 2 d.p.i., mRNA levels of *Ifn-β*, *Ifit1*, and *Cxcl10* in spleens were determined by real time-PCR. Data are means ± SD of three independent samples. *$p < 0.05$.

(Fig. 1C). However, the route of MV administration is an issue to be further investigated.

In MV-infected human epithelial cells, signals via RIG-I and MDA5 are essential for production of type I IFN (9, 10). Cells lacking the MAVS protein, a common adaptor molecule for RIG-I and MDA5, are unable to produce type I IFN in response to members of the Paramyxoviridae family (8). To investigate the in vivo role of the MAVS pathway during MV infection, we first examined whether CD150Tg/*Mavs*$^{-/-}$ mice were permissive to MV infection. Although luciferase activity in splenocytes was slightly increased in CD150Tg/*Mavs*$^{-/-}$ mice compared with CD150Tg mice 1 d after i.p. inoculation, luciferase activity in splenocytes of CD150Tg/*Mavs*$^{-/-}$ mice was decreased to the same degree as in those of CD150Tg mice a few days after inoculation (Fig. 1A, 1D, 1E). In contrast, luciferase activity in splenocytes was significantly increased in CD150Tg/*Ifnar*$^{-/-}$ and CD150Tg/*Irf3*$^{-/-}$/*Irf7*$^{-/-}$ mice compared with CD150Tg, CD150Tg/*Mavs*$^{-/-}$, or CD150Tg/*Ticam1*$^{-/-}$ mice 2 d after inoculation (Fig. 1D). We also examined luciferase activity in LNs and CD4$^+$, CD8$^+$, CD19$^+$, and CD11c$^+$ cells isolated from splenocytes of the mice. As shown in Fig. 1E, luciferase activity in these cells from MV-infected CD150Tg/*Mavs*$^{-/-}$ mice was much lower than in those from CD150Tg/*Ifnar*$^{-/-}$ mice. To investigate the reasons why CD150Tg/*Mavs*$^{-/-}$ mice were resistant to MV infection, we examined the expression level of mRNA coding antiviral protein in splenocytes (Fig. 1F). The expression of *Ifn-β* and two IFN-inducible genes, *Ifit1* and *Cxcl10*, was upregulated by MV infection in splenocytes from CD150Tg/*Mavs*$^{-/-}$ mice, but not in those from CD150Tg/*Ifnar*$^{-/-}$ and CD150Tg/*Irf3*$^{-/-}$/*Irf7*$^{-/-}$ mice (Fig. 1F). Type I IFN levels in sera were below the detection limit throughout the time course (data not shown). These data suggest that in vivo MV infection induces the expression of type I IFN and IFN-inducible genes to elicit resistance to MV infection in CD150Tg/*Mavs*$^{-/-}$. Moreover, type I IFN induction by in vivo MV infection occurs via the IRF3/IRF7-dependent and MAVS-independent pathway.

Next, we performed in vivo infection experiments using IFNAR Ab. Type I IFNR in CD150Tg/*Mavs*$^{-/-}$ mice was blocked by injecting 2.5 mg of the MAR1-5A3 mAb against IFNAR-1, 1 d before infection. This dose of Ab is reported to block antiviral effects of type I IFN in vivo (31). In MV-infected CD150Tg/*Mavs*$^{-/-}$ mice, blocking of IFNAR increased luciferase activity in LNs up to 180-fold, and in splenocytes up to 10-fold (Fig. 2A). Similarly, luciferase activity was increased up to 6-fold in CD19$^+$, 8-fold in CD4$^+$, 29-fold in CD8$^+$, and 17-fold in CD11c$^+$ cells by IFNAR blocking (Fig. 2B). These results indicate that CD150Tg/*Mavs*$^{-/-}$ mice are permissive to MV infection once IFNAR is functionally neutralized.

CD11c$^+$ DCs produce type I IFN via the MAVS-independent pathway during MV infection

To determine which cell types were responsible for type I IFN induction in MV-infected CD150Tg/*Mavs*$^{-/-}$ mice, we performed an in vitro infection assay using splenocytes. When infected with MV in vitro, the luciferase activity in B cells and T cells isolated from CD150Tg/*Mavs*$^{-/-}$ mice was comparable to activity in those from CD150Tg/*Ifnar*$^{-/-}$ mice (Fig. 3A). Treatment with anti-IFNAR Ab did not affect the infection efficiency in CD150Tg/*Mavs*$^{-/-}$ T and B cells (Fig. 3A). Unlike T and B cells, CD150Tg/*Mavs*$^{-/-}$ CD11c$^+$ DCs were not permissive to MV (Fig. 3A). These data suggest that CD11c$^+$ DCs, but not lymphocytes, are responsible for resistance to MV infection in CD150Tg/*Mavs*$^{-/-}$ mice. Because CD150Tg/*Mavs*$^{-/-}$ mice were permissive to MV in vivo when type I IFN signaling was blocked by anti-IFNAR Ab

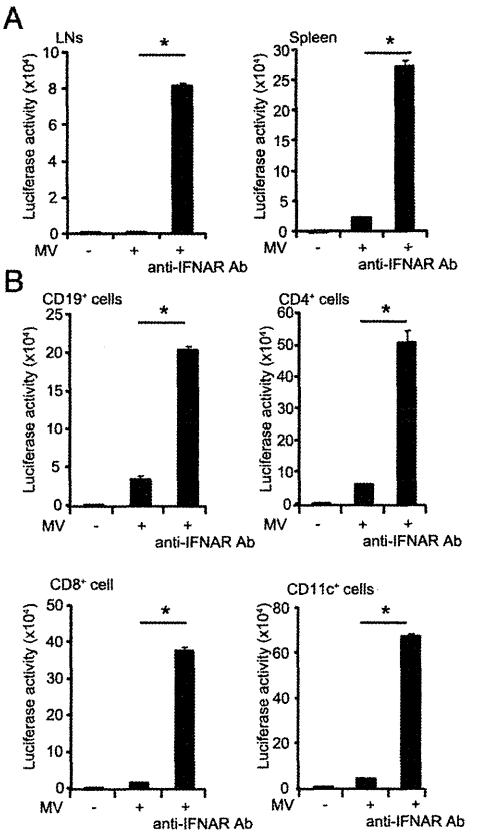

FIGURE 2. CD150Tg/*Mavs*$^{-/-}$ mice were permissive to MV after treatment with anti-IFNAR Ab in vivo. CD150Tg/*Mavs*$^{-/-}$ mice were injected i.p. with 2.5 mg of anti-IFNAR Ab at 1 d before MV-luciferase infection (1×10^7 PFU per mouse). At 2 d post infection, luciferase activity in LNs, splenocytes (**A**), and (**B**) CD19$^+$, CD4$^+$, CD8$^+$, and CD11c$^+$ cells isolated from splenocytes was measured and normalized by the total number of cells. Data are shown as the luciferase activity per 1×10^7 cells. Data are means ± SD of three independent samples. $^*p < 0.05$.

(Fig. 2A, 2B), we examined whether treatment with anti-IFNAR Ab increased the efficiency of MV infection in vitro. CD150Tg/*Mavs*$^{-/-}$ CD11c$^+$ DCs were permissive to MV in the presence of anti-IFNAR Ab (Fig. 3A). Consistent with results in Fig. 3A, type I IFN was detectable in the culture supernatant of MV-infected CD150Tg/*Mavs*$^{-/-}$ CD11c$^+$ DCs, but not of T or B cells (Fig. 3B and data not shown). Expression of *Ifn-β* and *Ifn-α4* mRNAs in CD150Tg/*Mavs*$^{-/-}$ CD11c$^+$ DCs was also upregulated within 6 h after MV infection (Fig. 3C). These data suggest that CD11c$^+$ DCs, but neither T nor B cells, mainly produce type I IFN through the MAVS-independent pathway in response to MV infection in vitro.

CD4$^+$ DCs and pDCs are responsible for MV-induced type I IFN production in CD150Tg/Mavs$^{-/-}$ *mice*

Our data indicate that type I IFN induction following the MV recognition in mouse DCs is independent of the MAVS pathway. Various types of DCs have been identified in mouse secondary lymphoid tissues, including three CD11c^{high} subsets: CD8α$^+$, CD4$^+$, and DN CD4$^-$CD8α$^-$ DCs (32), and one subset of CD11c^{low} pDCs (33). To identify the type I IFN-producing subsets, we used a cell sorter to isolate CD11c^{high} (cDCs) and CD11c^{low} pDCs from splenocytes, with purity > 98% (data not shown). CD150Tg/*Ifnar*$^{-/-}$ cDCs and pDCs were permissive to MV (Fig. 4A and 4C). In contrast, both CD150Tg/*Mavs*$^{-/-}$ cDCs and pDCs

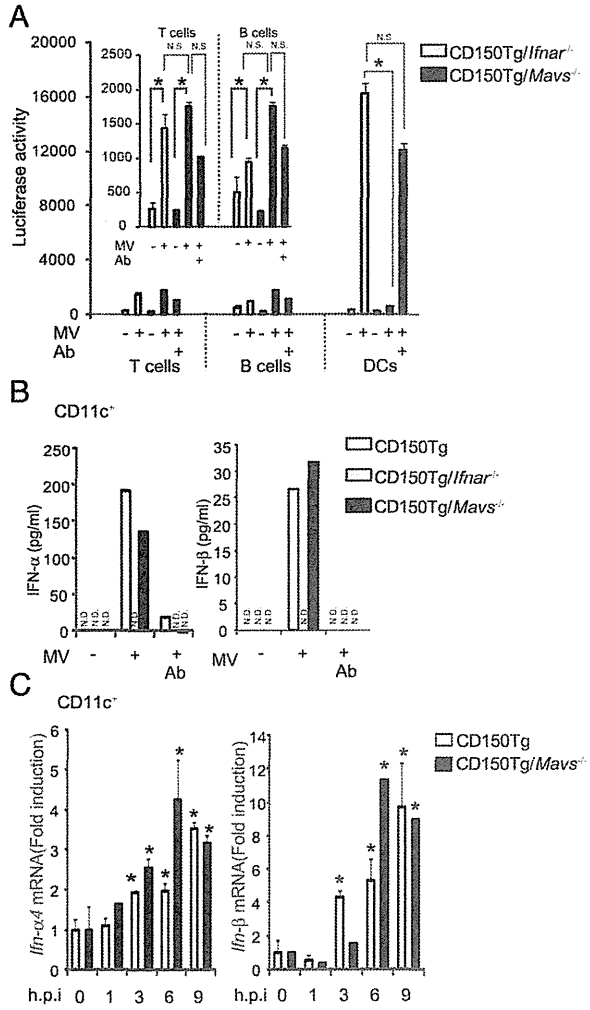

FIGURE 3. CD11c$^+$ DCs mainly produced type I IFN during MV infection in vitro. (**A**) T cells, B cells, and DCs were isolated from CD150Tg/*Ifnar*$^{-/-}$ and CD150Tg/*Mavs*$^{-/-}$ splenocytes, using MACS beads. Cells were treated with or without 10 μg/ml of anti-IFNAR Ab, then infected with mock or MV-luciferase at an MOI of 0.25. At 24 h post infection, luciferase activity was measured. Data are means ± SD of three independent samples. *$p < 0.05$. (**B**) CD11c$^+$ cells were prepared from splenocytes of CD150Tg, CD150Tg/*Ifnar*$^{-/-}$, and CD150Tg/*Mavs*$^{-/-}$ mice, using MACS beads. IFN-α and IFN-β protein production in culture supernatant of MV-infected cells (MOI = 0.25) was measured by ELISA. One of two experiments is shown. (**C**) CD11c$^+$ DCs were infected with MV (MOI of 0.25) for the indicated times, and type I IFN expression was determined by real-time PCR. Data are means ± SD of three independent samples. *A *t* test between 0 h.p.i. and the indicated time in respective mouse lines is $p < 0.05$. N.D., Not detected.

produced type I IFN (Fig. 4B, 4D) and were not permissive to MV (Fig. 4A, 4C). The resistance to MV infection was abolished by neutralizing type I IFNR with anti-IFNAR Ab (Fig. 4A, 4C). These data indicate that, like CD11c$^+$ DCs, CD150Tg/*Mavs*$^{-/-}$ pDCs and cDCs were barely permissive to MV because of the type I IFN production.

For more detailed study on the type I IFN-producing subsets, we further separated cDCs into CD8α$^+$, CD4$^+$, and DN DCs, using MACS beads. The purity of these subsets was > 90% (data not shown). *Ifn-β* mRNA was not induced in CD150Tg/*Mavs*$^{-/-}$ CD8α$^+$ DCs or DN DCs in response to MV infection (Fig. 5A, 5B). However, MV infection induced expression of *Ifn-β* mRNA in CD4$^+$ DCs from CD150Tg/*Mavs*$^{-/-}$ mice (Fig. 5C). Different from CD150Tg/*Mavs*$^{-/-}$ DCs, CD150Tg CD8α$^+$ and DN DCs expressed *Ifn-β* mRNA in response to MV infection (Fig. 5A, 5B). These data indicate that the expression of *Ifn-β* mRNA induced by MV infection is MAVS dependent in CD8α$^+$ DCs and DNs, but MAVS independent in CD4$^+$ DCs.

The MyD88-dependent pathway is essential for MV-induced type I IFN production in pDCs and CD4$^+$ DCs under MAVS deficiency

Next, we tried to identify the signaling pathway involved in type I IFN induction during MV infection. pDCs and CD4$^+$ DCs express TLR7 as a sensor for single-stranded RNA (34, 35). Recognition of single-stranded RNA through the TLR7-MyD88 pathway induces type I IFN expression in human and mouse pDCs (36–38). Therefore, we examined whether the TLR7-MyD88 pathway participated in the host defense during MV infection in mouse DCs. First, we analyzed the expression of TLR7 in pDCs and CD4$^+$ DCs. As reported in previous studies (34, 35), we were able to detect the expression of TLR7 at both mRNA and protein levels (Supplemental Fig. 2). RNA interference cannot be used in primary pDCs because the RNA molecules induce type I IFN expression (39); therefore, we used a peptide that is fused to an antennapedia-derived cell permeant motif and inhibits MyD88 homodimerization by binding to the MyD88 TIR domain (40). pDCs from wild-type mice were cultured for 6 h in the presence of the MyD88 inhibitory peptide or the control peptide and activated with R837, a TLR7 ligand, for 24 h. The control peptide marginally affected IFN-β secretion induced by R837, and the MyD88 inhibitory peptide at 50 μM significantly reduced IFN-β production induced by R837 (Supplemental Fig. 3A). To evaluate the effects of the inhibitory peptide on cell viability, we counted the number of live cells using trypan blue staining (Supplemental Fig. 3B). Although stimulation with R837 partially induced cell death (41.3% ± 5.4%), cell viability was not changed by the addition of the inhibitory peptide at 50 μM (Supplemental Fig. 3B). MyD88 inhibitory peptide has no effects on polyinosinic/polycytidylic acid–induced IFN-β production in CD11c$^+$ DCs (Supplemental Fig. 3C). Next, we tested the effect of MyD88 inhibitory peptide on permissiveness and type I IFN production in MV-infected pDCs from CD150Tg/*Mavs*$^{-/-}$ mice. Although CD150Tg/*Mavs*$^{-/-}$ pDCs were not permissive to MV in the presence of control peptide, infection efficiency was increased 4-fold by treatment with MyD88 inhibitory peptide (Fig. 6A). As with pDCs, the infection efficiency of CD150Tg/*Mavs*$^{-/-}$ CD11c$^+$ DCs increased 3-fold by MyD88 inhibitory peptide treatment (Fig. 6B). When CD150Tg/*Mavs*$^{-/-}$ CD11c$^+$ DCs, CD4$^+$ DCs, and pDCs were pretreated with MyD88 inhibitory peptide, they did not induce type I IFN mRNA after MV infection (Fig. 6C–E). These data suggest that the MyD88 pathway is responsible for MV-induced type I IFN production in DCs under MAVS deficiency. To confirm that the MyD88 pathway is involved in type I IFN induction in MV-infected DCs, CD150Tg/*Myd88*$^{-/-}$ pDCs were infected with MV in vitro. *Ifn-β* mRNA expression was not induced in MV-infected CD150Tg/*Myd88*$^{-/-}$ pDCs (Fig. 6F).

Discussion

This study demonstrated that CD150Tg/*Mavs*$^{-/-}$ mice were not susceptible to MV infection in vivo (Fig. 1). This is an unexpected result because many reports have highlighted the important role of the RIG-I/MDA5-MAVS pathway in type I IFN production in MV-infected cells as a means to suppress MV replication. Ultimately, the MyD88 signal, rather than the MAVS signal, serves as a critical inducer of primary type I IFN for cell protection against

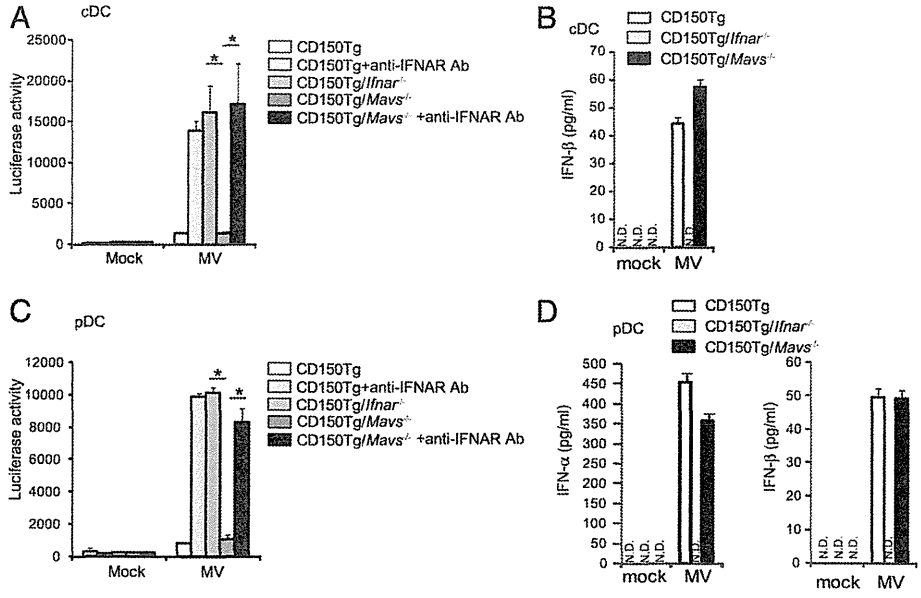

FIGURE 4. CD150Tg/*Mavs*$^{-/-}$ pDCs produced type I IFN in response to MV infection. The cDCs (**A**, **B**) or pDCs (**C**, **D**) isolated from CD150Tg, CD150Tg/*Ifnar*$^{-/-}$, or CD150Tg/*Mavs*$^{-/-}$ splenocytes were infected by MV (MOI of 0.25). At 24 h post infection, luciferase activity was measured (A, C). Production of type I IFN in culture supernatant was measured by ELISA (B, D). Data are means ± SD of three independent samples. N.D., Not detected.

MV replication in a mouse model. This finding would be a novel feature of MV, a negative single-stranded RNA virus, and has reminded us that cell-level studies on host innate immunity in coping with infection cannot always predict critical virus-sensing factors in whole-animal studies.

Because blockage of type I IFNR function resulted in permissiveness of CD150Tg/*Mavs*$^{-/-}$ mice to MV, MAVS-independent type I IFN induction protects neighboring cells (that express IFNAR) from MV infection (Fig. 2). Among the cell subsets tested, only pDCs and CD4$^+$ DCs from CD150Tg/*Mavs*$^{-/-}$ produced type I IFN after MV infection (Figs. 3–5). Treatment with inhibitory peptide for MyD88 drastically decreased type I IFN expression in CD150Tg/*Mavs*$^{-/-}$ DCs and rendered these cells MV permissive to MV (Fig. 6). These data indicate that the MyD88 pathway is involved in type I IFN induction in MV-infected pDCs and CD4$^+$ DCs under a MAVS-deficient state. The results were confirmed with CD150/*Myd88*$^{-/-}$ mice (Fig. 6F). In this context, the MyD88 pathway plays a primary role in the initial phase of MV protection in vivo. However, CD150Tg/*Myd88*$^{-/-}$ mice were not permissive to MV in vivo (data not shown), suggesting that not only MyD88 in pDCs/CD4$^+$ DCs but also MAVS in other cells contributes to the protection against systemic infection by MV. Because the MyD88 pathway participates in the initial type I IFN induction in pDCs, only a very weak but significant luciferase activity was detected in the spleen of CD150Tg/*Mavs*$^{-/-}$ mice at day 1 after inoculation (Fig. 1C). Moreover, CD8α$^+$ DCs and DN DCs from CD150Tg/*Mavs*$^{-/-}$ mice could not induce *Ifn-β* mRNA expression in response to MV infection in vitro (Fig. 5). These results suggest that the MAVS pathway also participates in host defense against MV infection as an alternative pathway in splenic DCs, at least in these experimental conditions.

Another target cell of MV infection in nonhuman primates is the AM (18). AMs in the CD150Tg/*Ifnar*$^{-/-}$ mouse model are also permissive to MV infection (17). AMs derived from CD150Tg/*Mavs*$^{-/-}$ mice were permissive to MV infection in vitro (data not shown). This result is consistent with a previous report indicating that the RLR-MAVS pathway is predominantly used for type I IFN induction in virus-infected AMs (41). However, intratracheal inoculation with MV in CD150Tg/*Mavs*$^{-/-}$ mice resulted in a lower luciferase activity in AMs from CD150Tg/*Mavs*$^{-/-}$ mice than in those from CD150Tg/*Ifnar*$^{-/-}$ mice (data not shown), similar to the results from i.p. inoculation. These data indicate that a cell population other than AMs produces type I IFN in MV-infected lungs. In this case, pDCs in lung might act as IFN-producing cells, because pDCs in lung are reported to produce type I IFN and act as immune system defenders against infection (41). Taken together, the recognition pathways for MV to induce type I IFN differ among cell types. Existence of the several alternative pathways might engage the protection from systemic MV infection (Supplemental Fig. 4).

In CD8α$^-$ DCs and pDCs, the TLR-MyD88 pathway is preferentially used to induce type I IFN in response to infections. TLR7, a sensor for viral RNA, is known to be expressed specifically in these DC subsets (34, 35) (Supplemental Fig. 2). The restricted expression pattern of TLR7 seems to reflect the ability of CD4$^+$ DCs and pDCs to produce type I IFN in MV-infected CD150Tg/*Mavs*$^{-/-}$. Therefore, TLR7 may be one of the candidate receptors for recognition of MV RNA. Because viral RNA is recognized mainly through the RLR-MAVS pathway in CD4$^+$ DCs at steady state (35), it would be difficult to examine the role of the TLR7-MyD88 pathway in CD4$^+$ DCs during viral infection in WT mice. Thus, our assay system using CD150Tg mice crossed with given knockout mice is a powerful tool to investigate the signaling pathway for host defense against MV infection.

Previous studies were mainly done using bone marrow–derived DCs (BMDCs) to analyze the immunosuppressive effects of MV in a mouse model (16, 42, 43). However, BMDCs from CD150Tg/*Mavs*$^{-/-}$ mice completely lacked the ability to produce type I IFN in response to MV infection. In contrast to the results in splenic DCs (44). Because the expression profile of pattern-recognition receptors in BMDCs was different from the profile in splenic DCs (34, 35, 45), it is reasonable to think that each cell type has its own unique type I IFN induction pathway in response to viral infection. Therefore, further investigations on immunosuppression and immunopromotion of MV in infected DCs should be performed using splenic DCs, taking into consideration the properties of resident DCs.

In this study, we used recombinant MV-luciferase that expresses the reporter *Renilla* luciferase from the first gene position of MV genome (29). The MV-luciferase is suitable to evaluate the efficiency of infection in vivo and in vitro correctly because the assay

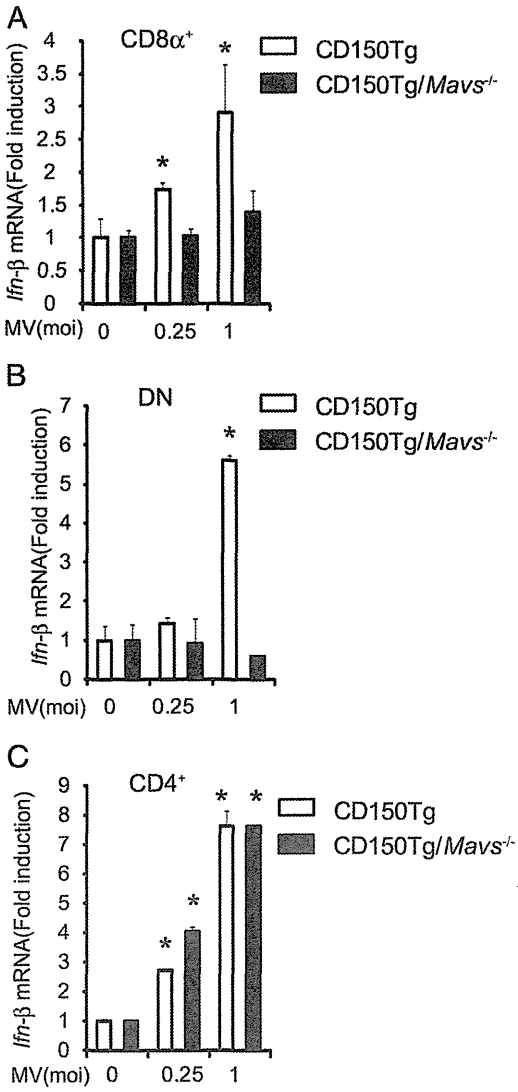

FIGURE 5. MV-infected CD150Tg/*Mavs*$^{-/-}$ CD4$^+$ DCs expressed type I IFN mRNA. CD8α$^+$ DCs (**A**), DN DCs (**B**), and CD4$^+$ DCs (**C**) were isolated by MACS beads. Cells were infected with MV (MOI of 0.25 or 1.0) for 9 h, and levels of *Ifn-β* mRNA were measured by real-time PCR. Data are means ± SD of three independent samples. *A *t* test between 0 h. p.i. and the indicate time in respective mouse line is $p < 0.05$.

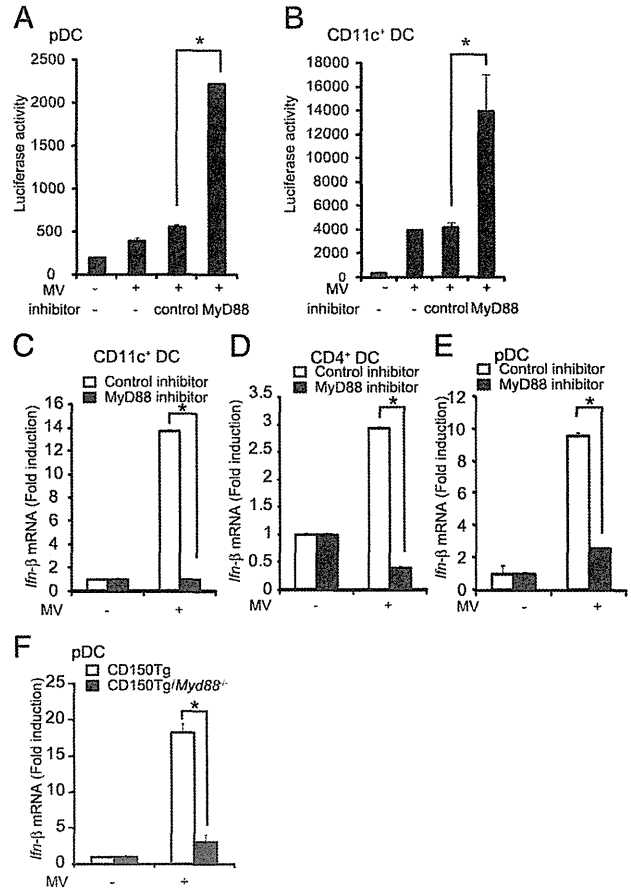

FIGURE 6. The MyD88 pathway is responsible for MV-induced type I IFN induction in CD150Tg/*Mavs*$^{-/-}$ DCs. (**A**) pDCs were isolated by FACS or (**B**) CD11c$^+$ DCs were isolated by MACS beads from CD150Tg/*Mavs*$^{-/-}$ splenocytes. Cells were treated with 50 μM of the control peptide or 50 μM of the MyD88 inhibitory peptide for 6 h and then infected with MV (MOI of 0.25). After 18 h, luciferase activity was measured. Data are means ± SD of three independent samples. CD150Tg/*Mavs*$^{-/-}$ CD11c$^+$ DCs (**C**), CD4$^+$ DCs (**D**), and pDCs (**E**) were pretreated with 50 μM control peptide or 50 μM MyD88 inhibitory peptide for 6 h following infection with MV (MOI of 0.25) for 9 h. Expression levels of *Ifn-β* mRNA were measured by real-time PCR. Expression levels of data are means ± SD of three independent samples. (**F**) *Ifn-β* mRNA expression in MV-infected CD150Tg and CD150Tg/*Myd88*$^{-/-}$ pDCs. pDCs were infected with MV (MOI = 0.25) for 9 h. Expression levels of *Ifn-β* mRNA were measured by real-time PCR. Expression levels of data are means ± SD of three independent samples. *$p < 0.05$.

system worked well using the CD150Tg/*Ifnar*$^{-/-}$ mouse model. Luciferase activity and MV-P mRNA in CD150Tg/*Ifnar*$^{-/-}$ was significantly increased compared with CD150Tg mice during infection (Fig. 1A, 1B and data not shown). Luciferase activity obtained from MV-infected Vero/CD150 cells was correlated with viral titer in culture supernatant from MV-infected cells (data not shown). Recombinant MV strains expressing a foreign gene from a first gene position of the MV genome were used in several groups for in vivo infection assay without any problem (17, 18, 24). However, the infection efficiency of recombinant *Morbillivirus* expressing a foreign gene from position one is reported to be attenuated in vivo (46), which is well reflected in the relatively low virus titer observed in the spleen from CD150Tg mice infected with MV-luciferase.

In mouse models, the route of MV inoculation does not always reflect the natural infection route in human MV infection. Our results obtained from experiments using the i.p. infection model also may not faithfully reflect the process of natural MV infection involving epithelial cells in humans. However, as described above, intratracheal and i.p. administration gave rise to similar results in MV infection. This issue may reflect the viral strategy of targeting myeloid cells for initial propagation. Injected MV reaches DCs or macrophages without affecting other bystander cells in any route of MV administration. However, this is not the case in other virus species with different target cells for initial infection.

We conclude that MyD88-dependent type I IFN production in CD4$^+$ DCs and pDCs results in initial protection against MV; thereafter, the produced type I IFN induces an antiviral state in the neighboring cells, expressing IFNAR in the mouse model.

Acknowledgments

We thank Drs. T. Taniguchi (University of Tokyo, Tokyo, Japan) and S. Akira (Osaka University, Osaka, Japan) for providing *Irf3*$^{-/-}$/*Irf7*$^{-/-}$ and *Myd88*$^{-/-}$ mice, respectively, for this study, and Dr. Y. Yanagi (Kyushu University, Fukuoka, Japan) for providing MV-luciferase.

Disclosures

The authors have no financial conflicts of interest.

References

1. Honda, K., A. Takaoka, and T. Taniguchi. 2006. Type I interferon [corrected] gene induction by the interferon regulatory factor family of transcription factors. *Immunity* 25: 349–360.
2. Yoneyama, M., K. Onomoto, and T. Fujita. 2008. Cytoplasmic recognition of RNA. *Adv. Drug Deliv. Rev.* 60: 841–846.
3. Takeuchi, O., and S. Akira. 2009. Innate immunity to virus infection. *Immunol. Rev.* 227: 75–86.
4. Yamamoto, M., S. Sato, K. Mori, K. Hoshino, O. Takeuchi, K. Takeda, and S. Akira. 2002. Cutting edge: a novel Toll/IL-1 receptor domain-containing adapter that preferentially activates the IFN-beta promoter in the Toll-like receptor signaling. *J. Immunol.* 169: 6668–6672.
5. Oshiumi, H., M. Matsumoto, K. Funami, T. Akazawa, and T. Seya. 2003. TICAM-1, an adaptor molecule that participates in Toll-like receptor 3-mediated interferon-beta induction. *Nat. Immunol.* 4: 161–167.
6. Kawai, T., K. Takahashi, S. Sato, C. Coban, H. Kumar, H. Kato, K. J. Ishii, O. Takeuchi, and S. Akira. 2005. IPS-1, an adaptor triggering RIG-I- and Mda5-mediated type I interferon induction. *Nat. Immunol.* 6: 981–988.
7. Yamamoto, M., S. Sato, H. Hemmi, K. Hoshino, T. Kaisho, H. Sanjo, O. Takeuchi, M. Sugiyama, M. Okabe, K. Takeda, and S. Akira. 2003. Role of adaptor TRIF in the MyD88-independent toll-like receptor signaling pathway. *Science* 301: 640–643.
8. Kumar, H., T. Kawai, H. Kato, S. Sato, K. Takahashi, C. Coban, M. Yamamoto, S. Uematsu, K. J. Ishii, O. Takeuchi, and S. Akira. 2006. Essential role of IPS-1 in innate immune responses against RNA viruses. *J. Exp. Med.* 203: 1795–1803.
9. Ikegame, S., M. Takeda, S. Ohno, Y. Nakatsu, Y. Nakanishi, and Y. Yanagi. 2010. Both RIG-I and MDA5 RNA helicases contribute to the induction of alpha/beta interferon in measles virus-infected human cells. *J. Virol.* 84: 372–379.
10. Berghäll, H., J. Sirén, D. Sarkar, I. Julkunen, P. B. Fisher, R. Vainionpää, and S. Matikainen. 2006. The interferon-inducible RNA helicase, mda-5, is involved in measles virus-induced expression of antiviral cytokines. *Microbes Infect.* 8: 2138–2144.
11. Griffin, D. E. 1995. Immune responses during measles virus infection. *Curr. Top. Microbiol. Immunol.* 191: 117–134.
12. Tatsuo, H., N. Ono, K. Tanaka, and Y. Yanagi. 2000. SLAM (CDw150) is a cellular receptor for measles virus. *Nature* 406: 893–897.
13. Mühlebach, M. D., M. Mateo, P. L. Sinn, S. Prüfer, K. M. Uhlig, V. H. Leonard, C. K. Navaratnarajah, M. Frenzke, X. X. Wong, B. Sawatsky, et al. 2011. Adherens junction protein nectin-4 is the epithelial receptor for measles virus. *Nature* 480: 530–533.
14. Noyce, R. S., D. G. Bondre, M. N. Ha, L. T. Lin, G. Sisson, M. S. Tsao, and C. D. Richardson. 2011. Tumor cell marker PVRL4 (nectin 4) is an epithelial cell receptor for measles virus. *PLoS Pathog.* 7: e1002240.
15. Delpeut, S., R. S. Noyce, R. W. Siu, and C. D. Richardson. 2012. Host factors and measles virus replication. *Curr Opin Virol* 2: 773–783.
16. Shingai, M., N. Inoue, T. Okuno, M. Okabe, T. Akazawa, Y. Miyamoto, M. Ayata, K. Honda, M. Kurita-Taniguchi, M. Matsumoto, et al. 2005. Wild-type measles virus infection in human CD46/CD150-transgenic mice: CD11c-positive dendritic cells establish systemic viral infection. *J. Immunol.* 175: 3252–3261.
17. Ferreira, C. S., M. Frenzke, V. H. Leonard, G. G. Welstead, C. D. Richardson, and R. Cattaneo. 2010. Measles virus infection of alveolar macrophages and dendritic cells precedes spread to lymphatic organs in transgenic mice expressing human signaling lymphocytic activation molecule (SLAM, CD150). *J. Virol.* 84: 3033–3042.
18. Lemon, K., R. D. de Vries, A. W. Mesman, S. McQuaid, G. van Amerongen, S. Yüksel, M. Ludlow, L. J. Rennick, T. Kuiken, B. K. Rima, et al. 2011. Early target cells of measles virus after aerosol infection of non-human primates. *PLoS Pathog.* 7: e1001263.
19. Mesman, A. W., R. D. de Vries, S. McQuaid, W. P. Duprex, R. L. de Swart, and T. B. Geijtenbeek. 2012. A prominent role for DC-SIGN+ dendritic cells in initiation and dissemination of measles virus infection in non-human primates. *PLoS ONE* 7: e49573.
20. Schneider-Schaulies, S., I. M. Klagge, and V. ter Meulen. 2003. Dendritic cells and measles virus infection. *Curr. Top. Microbiol. Immunol.* 276: 77–101.
21. Servet-Delprat, C., P. O. Vidalain, H. Valentin, and C. Rabourdin-Combe. 2003. Measles virus and dendritic cell functions: how specific response cohabits with immunosuppression. *Curr. Top. Microbiol. Immunol.* 276: 103–123.
22. Welstead, G. G., C. Iorio, R. Draker, J. Bayani, J. Squire, S. Vongpunsawad, R. Cattaneo, and C. D. Richardson. 2005. Measles virus replication in lymphatic cells and organs of CD150 (SLAM) transgenic mice. *Proc. Natl. Acad. Sci. USA* 102: 16415–16420.
23. Sellin, C. I., N. Davoust, V. Guillaume, D. Baas, M. F. Belin, R. Buckland, T. F. Wild, and B. Horvat. 2006. High pathogenicity of wild-type measles virus infection in CD150 (SLAM) transgenic mice. *J. Virol.* 80: 6420–6429.
24. Ohno, S., N. Ono, F. Seki, M. Takeda, S. Kura, T. Tsuzuki, and Y. Yanagi. 2007. Measles virus infection of SLAM (CD150) knockin mice reproduces tropism and immunosuppression in human infection. *J. Virol.* 81: 1650–1659.
25. Akazawa, T., T. Ebihara, M. Okuno, Y. Okuda, M. Shingai, K. Tsujimura, T. Takahashi, M. Ikawa, M. Okabe, N. Inoue, et al. 2007. Antitumor NK activation induced by the Toll-like receptor 3-TICAM-1 (TRIF) pathway in myeloid dendritic cells. *Proc. Natl. Acad. Sci. USA* 104: 252–257.
26. Oshiumi, H., M. Okamoto, K. Fujii, T. Kawanishi, M. Matsumoto, S. Koike, and T. Seya. 2011. The TLR3/TICAM-1 pathway is mandatory for innate immune responses to poliovirus infection. *J. Immunol.* 187: 5320–5327.
27. Kobune, F., H. Sakata, and A. Sugiura. 1990. Marmoset lymphoblastoid cells as a sensitive host for isolation of measles virus. *J. Virol.* 64: 700–705.
28. Takeda, M., K. Takeuchi, N. Miyajima, F. Kobune, Y. Ami, N. Nagata, Y. Suzaki, Y. Nagai, and M. Tashiro. 2000. Recovery of pathogenic measles virus from cloned cDNA. *J. Virol.* 74: 6643–6647.
29. Takeda, M., M. Tahara, T. Hashiguchi, T. A. Sato, F. Jinnouchi, S. Ueki, S. Ohno, and Y. Yanagi. 2007. A human lung carcinoma cell line supports efficient measles virus growth and syncytium formation via a SLAM- and CD46-independent mechanism. *J. Virol.* 81: 12091–12096.
30. Shingai, M., T. Ebihara, N. A. Begum, A. Kato, T. Honma, K. Matsumoto, H. Saito, H. Ogura, M. Matsumoto, and T. Seya. 2007. Differential type I IFN-inducing abilities of wild-type versus vaccine strains of measles virus. *J. Immunol.* 179: 6123–6133.
31. Sheehan, K. C., K. S. Lai, G. P. Dunn, A. T. Bruce, M. S. Diamond, J. D. Heutel, C. Dungo-Arthur, J. A. Carrero, J. M. White, P. J. Hertzog, and R. D. Schreiber. 2006. Blocking monoclonal antibodies specific for mouse IFN-alpha/beta receptor subunit 1 (IFNAR-1) from mice immunized by in vivo hydrodynamic transfection. *J. Interferon Cytokine Res.* 26: 804–819.
32. Vremec, D., J. Pooley, H. Hochrein, L. Wu, and K. Shortman. 2000. CD4 and CD8 expression by dendritic cell subtypes in mouse thymus and spleen. *J. Immunol.* 164: 2978–2986.
33. Asselin-Paturel, C., A. Boonstra, M. Dalod, I. Durand, N. Yessaad, C. Dezutter-Dambuyant, A. Vicari, A. O'Garra, C. Biron, F. Brière, and G. Trinchieri. 2001. Mouse type I IFN-producing cells are immature APCs with plasmacytoid morphology. *Nat. Immunol.* 2: 1144–1150.
34. Edwards, A. D., S. S. Diebold, E. M. Slack, H. Tomizawa, H. Hemmi, T. Kaisho, S. Akira, and C. Reis e Sousa. 2003. Toll-like receptor expression in murine DC subsets: lack of TLR7 expression by CD8 alpha+ DC correlates with unresponsiveness to imidazoquinolines. *Eur. J. Immunol.* 33: 827–833.
35. Luber, C. A., J. Cox, H. Lauterbach, B. Fancke, M. Selbach, J. Tschopp, S. Akira, M. Wiegand, H. Hochrein, M. O'Keeffe, and M. Mann. 2010. Quantitative proteomics reveals subset-specific viral recognition in dendritic cells. *Immunity* 32: 279–289.
36. Hemmi, H., T. Kaisho, O. Takeuchi, S. Sato, H. Sanjo, K. Hoshino, T. Horiuchi, H. Tomizawa, K. Takeda, and S. Akira. 2002. Small anti-viral compounds activate immune cells via the TLR7 MyD88-dependent signaling pathway. *Nat. Immunol.* 3: 196–200.
37. Heil, F., H. Hemmi, H. Hochrein, F. Ampenberger, C. Kirschning, S. Akira, G. Lipford, H. Wagner, and S. Bauer. 2004. Species-specific recognition of single-stranded RNA via toll-like receptor 7 and 8. *Science* 303: 1526–1529.
38. Diebold, S. S., T. Kaisho, H. Hemmi, S. Akira, and C. Reis e Sousa. 2004. Innate antiviral responses by means of TLR7-mediated recognition of single-stranded RNA. *Science* 303: 1529–1531.
39. Hornung, V., M. Guenthner-Biller, C. Bourquin, A. Ablasser, M. Schlee, S. Uematsu, A. Noronha, M. Manoharan, S. Akira, A. de Fougerolles, et al. 2005. Sequence-specific potent induction of IFN-alpha by short interfering RNA in plasmacytoid dendritic cells through TLR7. *Nat. Med.* 11: 263–270.
40. Loiarro, M., C. Sette, G. Gallo, A. Ciacci, N. Fantò, D. Mastroianni, P. Carminati, and V. Ruggiero. 2005. Peptide-mediated interference of TIR domain dimerization in MyD88 inhibits interleukin-1-dependent activation of NF-kappaB. *J. Biol. Chem.* 280: 15809–15814.
41. Kumagai, Y., O. Takeuchi, H. Kato, H. Kumar, K. Matsui, E. Morii, K. Aozasa, T. Kawai, and S. Akira. 2007. Alveolar macrophages are the primary interferon-alpha producer in pulmonary infection with RNA viruses. *Immunity* 27: 240–252.
42. Hahm, B., N. Arbour, and M. B. Oldstone. 2004. Measles virus interacts with human SLAM receptor on dendritic cells to cause immunosuppression. *Virology* 323: 292–302.
43. Koga, R., S. Ohno, S. Ikegame, and Y. Yanagi. 2010. Measles virus-induced immunosuppression in SLAM knock-in mice. *J. Virol.* 84: 5360–5367.
44. Takaki, H., K. Honda, K. Atarashi, F. Kobayashi, T. Ebihara, H. Oshiumi, M. Matsumoto, M. Shingai, and T. Seya. 2013. MAVS-dependent IRF3/IRF7 bypass of interferon β-induction restricts the response to measles infection in CD150Tg mouse bone marrow-derived dendritic cells. *Molec. Immunol.* In press.
45. Datta, S. K., V. Redecke, K. R. Prilliman, K. Takabayashi, M. Corr, T. Tallant, J. DiDonato, R. Dziarski, S. Akira, S. P. Schoenberger, and E. Raz. 2003. A subset of Toll-like receptor ligands induces cross-presentation by bone marrow-derived dendritic cells. *J. Immunol.* 170: 4102–4110.
46. von Messling, V., D. Milosevic, and R. Cattaneo. 2004. Tropism illuminated: lymphocyte-based pathways blazed by lethal morbillivirus through the host immune system. *Proc. Natl. Acad. Sci. USA* 101: 14216–14221.

OPEN ACCESS Freely available online

PLOS | PATHOGENS

A Distinct Role of Riplet-Mediated K63-Linked Polyubiquitination of the RIG-I Repressor Domain in Human Antiviral Innate Immune Responses

Hiroyuki Oshiumi*, Moeko Miyashita¤, Misako Matsumoto, Tsukasa Seya

Department of Microbiology and Immunology, Graduate School of Medicine, Hokkaido University, Kita-ku, Sapporo, Japan

Abstract

The innate immune system is essential for controlling viral infections, but several viruses have evolved strategies to escape innate immunity. RIG-I is a cytoplasmic viral RNA sensor that triggers the signal to induce type I interferon production in response to viral infection. RIG-I activation is regulated by the K63-linked polyubiquitin chain mediated by Riplet and TRIM25 ubiquitin ligases. TRIM25 is required for RIG-I oligomerization and interaction with the IPS-1 adaptor molecule. A knockout study revealed that Riplet was essential for RIG-I activation. However the molecular mechanism underlying RIG-I activation by Riplet remains unclear, and the functional differences between Riplet and TRIM25 are also unknown. A genetic study and a pull-down assay indicated that Riplet was dispensable for RIG-I RNA binding activity but required for TRIM25 to activate RIG-I. Mutational analysis demonstrated that Lys-788 within the RIG-I repressor domain was critical for Riplet-mediated K63-linked polyubiquitination and that Riplet was required for the release of RIG-I autorepression of its N-terminal CARDs, which leads to the association of RIG-I with TRIM25 ubiquitin ligase and TBK1 protein kinase. Our data indicate that Riplet is a prerequisite for TRIM25 to activate RIG-I signaling. We investigated the biological importance of this mechanism in human cells and found that hepatitis C virus (HCV) abrogated this mechanism. Interestingly, HCV NS3-4A proteases targeted the Riplet protein and abrogated endogenous RIG-I polyubiquitination and association with TRIM25 and TBK1, emphasizing the biological importance of this mechanism in human antiviral innate immunity. In conclusion, our results establish that Riplet-mediated K63-linked polyubiquitination released RIG-I RD autorepression, which allowed the access of positive factors to the RIG-I protein.

Citation: Oshiumi H, Miyashita M, Matsumoto M, Seya T (2013) A Distinct Role of Riplet-Mediated K63-Linked Polyubiquitination of the RIG-I Repressor Domain in Human Antiviral Innate Immune Responses. PLoS Pathog 9(8): e1003533. doi:10.1371/journal.ppat.1003533

Editor: Michael Gale Jr, University of Washington, United States of America

Received January 30, 2013; **Accepted** June 17, 2013; **Published** August 8, 2013

Funding: This work was supported in part by a grant-in-aid from the Ministry of Education, Science and Culture of Japan, and the Ministry of Health Labour, and Welfare of Japan, Kato Memorial Bioscience Foundation. The funders had no role in study design, data collection and analysis, decision to publish, or preparation of the manuscript.

Competing Interests: The authors have declared that no competing interests exist.

* E-mail: oshiumi@med.hokudai.ac.jp

¤ Current address: Hokkaido Pharmaceutical University School of Pharmacy, Katsuraoka-cho, Otaru, Hokkaido, Japan.

Introduction

The innate immune system is essential for controlling virus infections, and several viruses have evolved strategies to evade host innate immune responses. Cytoplasmic viral RNA is recognized by RIG-I-like receptors, including RIG-I and MDA5 [1,2]. The RIG-I protein comprises N-terminal Caspase Activation and Recruitment Domains (CARDs), a central RNA helicase domain, and a C-terminal Repressor domain (RD) [3]. RD consists of C-terminal RNA binding domain (CTD) and a bridging domain between CTD and helicase [4]. RIG-I CARDs are essential for triggering the signal that induces type I interferon (IFN). In resting cells, RIG-I RD represses its CARDs signaling [3]. After viral infection, RIG-I RD recognizes 5′-triphosphate double-stranded RNA (dsRNA), which results in a conformational change in the RIG-I protein [3]. This conformational change leads to the release of RD autorepression of CARDs, after which CARDs associate with an IPS-1 adaptor molecule (also called MAVS, Cardif, and VISA) localized at the outer membrane of mitochondria [3,5,6,7,8]. IPS-1 activates downstream factors such as TBK1, IKK-ε, and NEMO [9,10,11]. NEMO forms a complex with TBK1 and IKK-ε and has a polyubiquitin binding region [12]. These protein kinases are essential for activating transcription factors such as IRF-3 to induce type I IFN production [13].

Several ubiquitin ligases are involved in regulating the RIG-I-dependent pathway, and RIG-I itself is regulated by ubiquitin chains [14]. Gack MU and colleagues firstly reported that TRIM25 ubiquitin ligase mediates K63-linked polyubiquitination of RIG-I N-terminal CARDs, which results in RIG-I activation [15]. Other groups also detected a RIG-I-anchored polyubiquitin chain after ligand stimulation or viral infection [16,17]. It was recently demonstrated that an unanchored polyubiquitin chain but not ubiquitination is essential for RIG-I activation [18,19]. However, RIG-I anchored K63-linked polyubiquitin chains are detected after viral infection [15,20].

Another E3 ubiquitin ligase, Riplet, binds RIG-I RD and mediates the K63-linked polyubiquitination of RIG-I RD [21]. In contrast, Chen DY and colleagues reported that Riplet (also called Reul) ubiquitinated RIG-I CARDs [22]. A study that used Riplet knockout mice showed that mouse Riplet is essential for RIG-I-

Author Summary

The cytoplasmic viral RNA sensor RIG-I recognizes various types of pathogenic viruses and evokes innate immune responses, whereas several viruses have evolved strategies to escape the host innate immune responses. RIG-I triggers a signal to induce type I interferon and inflammatory cytokines. RIG-I activation is regulated by K63-linked polyubiquitin chains mediated by the ubiquitin ligases TRIM25 and Riplet; however, the functional difference between the two ubiquitin ligases remains unclear, and the molecular mechanism underlying Riplet-mediated RIG-I activation is unknown. We revealed sequential roles of the two ubiquitin ligases during RIG-I activation and found that Riplet-mediated polyubiquitination of the RIG-I repressor domain released RIG-I autorepression of its N-terminal CARDs responsible for triggering the signal, which resulted in an association with TRIM25 ubiquitin ligase and TBK1 protein kinase. Interestingly, we found that this mechanism was targeted by hepatitis C virus, which is a major cause of hepatocellular carcinoma. This result emphasizes the vital role of Riplet-mediated release of RIG-I RD autorepression in antiviral responses. Our results establish that Riplet releases RIG-I RD autorepression and demonstrated the biological significance of this mechanism in human innate immune responses.

mediated type I IFN production in response to vesicular stomatitis virus (VSV), Flu, and Sendai virus (SeV) infections [23]. However, the functional difference between Riplet and TRIM25 remains unclear, and the molecular mechanism of how Riplet-mediated RIG-I ubiquitination activates RIG-I signaling remains unresolved.

Hepatitis C virus (HCV) is a major cause of hepatocellular carcinoma (HCC) worldwide. HCV RNA is primarily recognized by RIG-I *in vitro* and *in vivo* [24]. The HCV protease NS3-4A can suppress type I IFN production [25]. NS3-4A cleaves IPS-1 to suppress RIG-I-mediated innate immune responses [7,26]. Human monocyte-derived dendritic cells recognize HCV RNA through Toll-like receptor 3, and NS3-4A has the ability to cleave TICAM-1, which is a solo adaptor molecule of Toll-like receptor 3 [27,28]. In this study, we found that Riplet was another target of NS3-4A. Here, we demonstrated the molecular mechanisms of how Riplet-mediated RIG-I polyubiquitination triggered the type I IFN production signal and showed that this mechanism was targeted by HCV.

Results

Riplet and TRIM25 ubiquitin ligases play different roles in RIG-I activation

In mouse embryonic fibroblasts (MEFs), TRIM25 is essential for type I IFN production in response to SeV infection [15]. As with TRIM25 knockout, Riplet knockout abolished IFN-α2 and IFN-β mRNA expressions in response to SeV infection in MEF (Figure 1A and 1B), which suggested that both ubiquitin ligases were essential for type I IFN expression in MEFs in response to SeV infection. Thus, we examined whether these two ubiquitin ligases played different roles in RIG-I activation.

We performed reporter gene assays with p125luc (IFN-β reporter) using either RIG-I CARDs fragment or full-length RIG-I expression vectors. It is known that ectopic expression of RIG-I CARDs fragment activates the signaling even in the absence of stimulation with RIG-I ligand [2,3] and that the autoactivation is observed when full-length RIG-I is ectopically expressed in HEK293 cell [21,29]. As previously reported, TRIM25 ectopic expression efficiently increased RIG-I CARDs fragment-mediated signaling (Figure 1C). However, TRIM25 expression only mildly increased full-length RIG-I signaling (Figure 1D). In contrast, Riplet ectopic expression efficiently increased the full-length RIG-I-mediated signaling, although Riplet failed to increase the RIG-I CARDs-mediated signaling (Figure 1C and 1D). Interestingly, when Riplet was co-expressed with TRIM25, ectopically expressed TRIM25 could increase the full-length RIG-I-mediated signaling (Figure 1F). We observed the same effects of TRIM25 and Riplet expressions on the reporter activation in the presence of stimulation with HCV 3′ UTR dsRNA (a RIG-I ligand) or VSV infection, which are recognized by RIG-I (Figure 1E and 1F). These different effects of Riplet and TRIM25 on the signaling suggested that Riplet and TRIM25 ubiquitin ligases played different roles in RIG-I activation.

We then investigated whether the two ubiquitin ligases associate with RIG-I after stimulation. First, we performed immunoprecipitation assay and found that endogenous Riplet and TRIM25 bound to endogenous RIG-I after stimulation with HCV dsRNA (Figure 1G). Second, we investigated subcellular localizations of the proteins by confocal immunofluorescence microscopy. In resting cells, RIG-I was barely detectable, whereas RIG-I exhibited punctate staining in cytoplasm after VSV infection (Figure 2A), and ectopically expressed Riplet was co-localized with RIG-I and TRIM25 in perinuclear region in VSV infected cells (Figure 2A–2C and 2E). This is consistent with a previous observation that RIG-I and TRIM25 co-localized extensively at cytoplasmic perinuclear bodies [15]. Pearson's correlation coefficient values also suggested the correlation of the colocalizations of those proteins (Figure 2D and 2F). Recently, it was reported that RIG-I recognized short polyI:C in stress granules [30]. G3BP is a marker of the stress granule [30]. In resting cells, G3BP dispersed in cytoplasm [30], and thus barely detectable (Figure 2G and 2H), whereas G3BP speckles were detected in cells stimulated with short polyI:C in the cytoplasm (Figure 2G and 2H). Riplet and TRIM25 localizations within G3BP speckles were detected in the stimulated cells (Figure 2G and 2H). Taken together, these data indicated that both Riplet and TRIM25 associated with RIG-I after stimulation.

Next, we assessed the RIG-I regions that bind to the two ubiquitin ligases using RIG-I fragments. As previously reported, TRIM25 bound to RIG-I CARDs fragment (Figure 2I). However, Riplet bound to RIG-I RD (735–925 aa), but not to CARDs fragment (Figure 2J). Deleting the Riplet binding region (RIG-I-ΔCTD) abrogated Riplet effect on RIG-I signaling (Figure 2K). This was contrast to TRIM25, which affects RIG-I CARDs. Taken together, our genetic and biochemical data indicated that the two ubiquitin ligases associated with RIG-I after stimulation but showed different effects on RIG-I activation. Thus, we next focused on Riplet specific role in RIG-I activation.

Riplet-mediated RIG-I polyubiquitination is dispensable for RIG-I RNA binding activity

RIG-I CARDs harbor K63-linked polyubiquitination [15]. As RIG-I CARDs, RIG-I RD harbored K63-linked polyubiquitination (Supplemental Figure S1). Riplet expression increased the polyubiquitination of RIG-I RD but not that of CARDs (Figure 3A). RIG-I RD has two functions. One is RNA binding activity and the other is autorepression of its CARDs signaling. Firstly, we tested whether Riplet affects RIG-I RNA binding activity. In a pull-down assay using biotin-conjugated dsRNA and streptavidin beads, we found that both polyubiquitinated and non-ubiquitinated RIG-I were recovered (Figure 3B), which suggested that Riplet-mediated polyubiquitination was dispensable for RIG-I

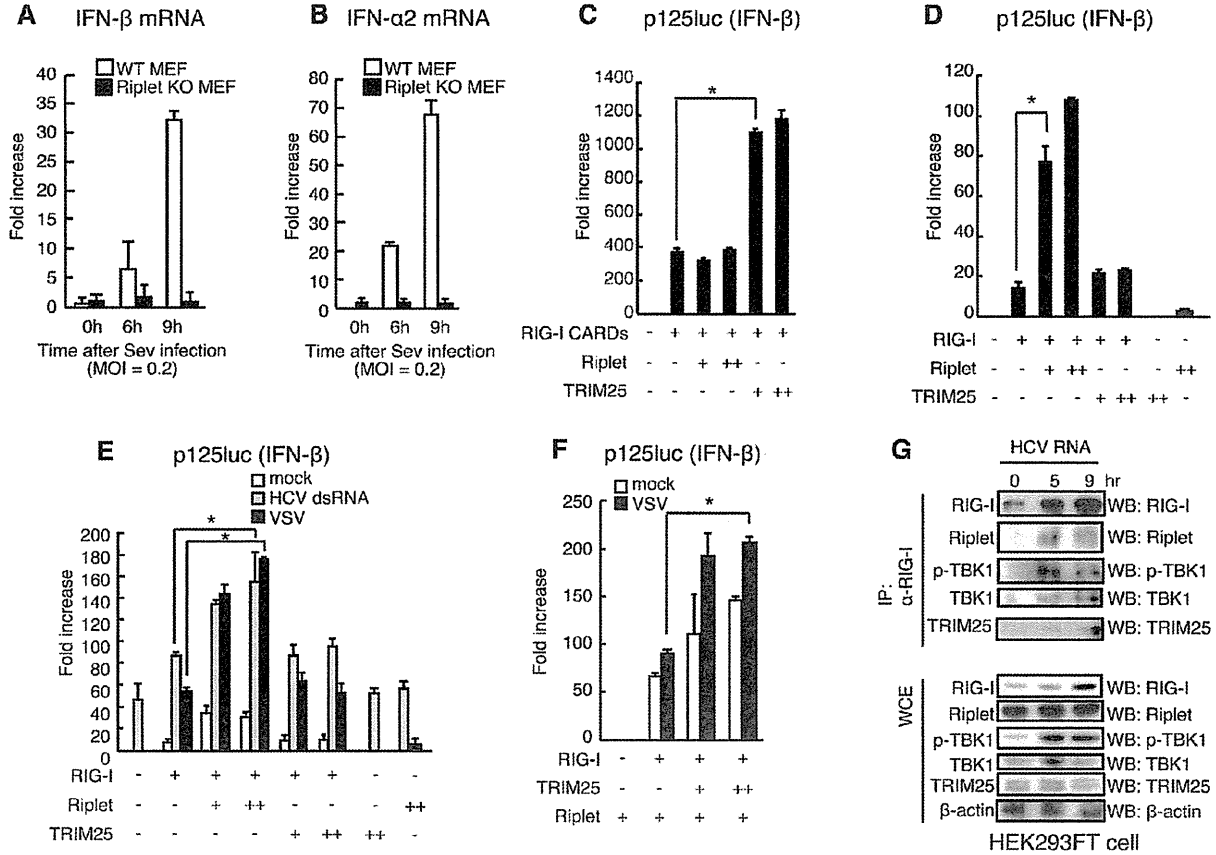

Figure 1. Riplet promotes TRIM25-mediated full-length RIG-I activation. (A, B) Wild-type and Riplet KO MEFs were infected with SeV at MOI = 0.2. The mRNA expressions of IFN-β (A) and -α2 (B) at the indicated times after viral infection were determined by RT-qPCR. Results are presented as mean ± SD (n = 3). (C, D) The activation of IFN-β promoter was examined by reporter gene assay using a p125luc IFN-β reporter. RIG-I CARDs (C) or full-length RIG-I (D) expression vectors were transfected into HEK293 cells together with a Riplet and/or TRIM25 expression vector as indicated. 24 hours after the transfection, the reporter activities were determined. (E, F) The activation of IFN-β promoter was examined by reporter gene assay using a p125luc IFN-β reporter. Full-length RIG-I expression vectors were transfected into HEK293 cells together with a Riplet and/or TRIM25 expression vector as indicated. 24 hours after the transfection, the cells were stimulated with 50 ng of HCV 3′ UTR dsRNA by transfection or infected with VSV at MOI = 1 for 24 hours, and then reporter activation was determined. Data are presented as mean ± SD (n = 3). *$p<0.05$. (G) HEK293FT cells were stimulated with 0.8 μg of HCV double-stranded RNA (HCV RNA) using lipofectamine 2000 in 6-well plate. Cell lysates were prepared at the indicated times, followed by immunoprecipitation with an anti-RIG-I mAb (Alme-1).
doi:10.1371/journal.ppat.1003533.g001

RNA binding activity. As RIG-I is known to form homo-oligomers [3], it is possible that non-ubiquitinated RIG-I was recovered through ubiquitinated RIG-I by the pull-down assay. To exclude this possibility, we used RIG-I mutants, RIG-I 5KR and RIG-I K788R, which were barely ubiquitinated by Riplet (described below). We compared the binding abilities of the RIG-I mutants to that of wild-type RIG-I by pull-down assay using cell lysate isolated from cells without stimulation with RIG-I ligand to avoid any ubiquitination. The results showed that the RIG-I 5KR and RIG-I K788R mutant proteins were recovered by pull down assay as wild-type RIG-I (Figure 3C). This data also indicated that the polyubiquitination is dispensable for RIG-I RNA binding activity.

Riplet releases RIG-I RD autorepression of CARDs signaling

Secondly, we investigated whether Riplet expression affects RIG-I RD autorepression of CARDs signaling. To test this possibility, we constructed RIG-I mutant proteins (Figure 4A). We previously showed that Lys to Ala amino acid substitutions at Lys-849, 851, 888, 907, and 909 of RIG-I (RIG-I 5KA) severely reduced RIG-I polyubiquitination and activation [21]. However, it is possible that the substitutions of Lys with Ala affect other function of RIG-I because the substitution abolishes positive charge of Lys residues. Thus, we constructed the RIG-I 5KR mutant protein, in which the five Lys residues were substituted with Arg, and examined the signal activation ability. The results showed that the 5KR mutation reduced RIG-I signaling, however residual activation of RIG-I 5KR was still detected (Figure 4B–4D). Thus, we assessed other Lys residues within RIG-I RD. Because Riplet is essential for RIG-I activation, it is expected that the Lys residues targeted by Riplet are conserved during evolution. Thus, we tested Lys residues within RIG-I RD conserved among vertebrate, and found that an RIG-I K788R mutation reduced RIG-I signaling at a level comparable to that by a K172R mutation, which abrogates TRIM25-mediated RIG-I activation [15,19] (Figure 4B–4D). Interestingly, the 5KR and K788R

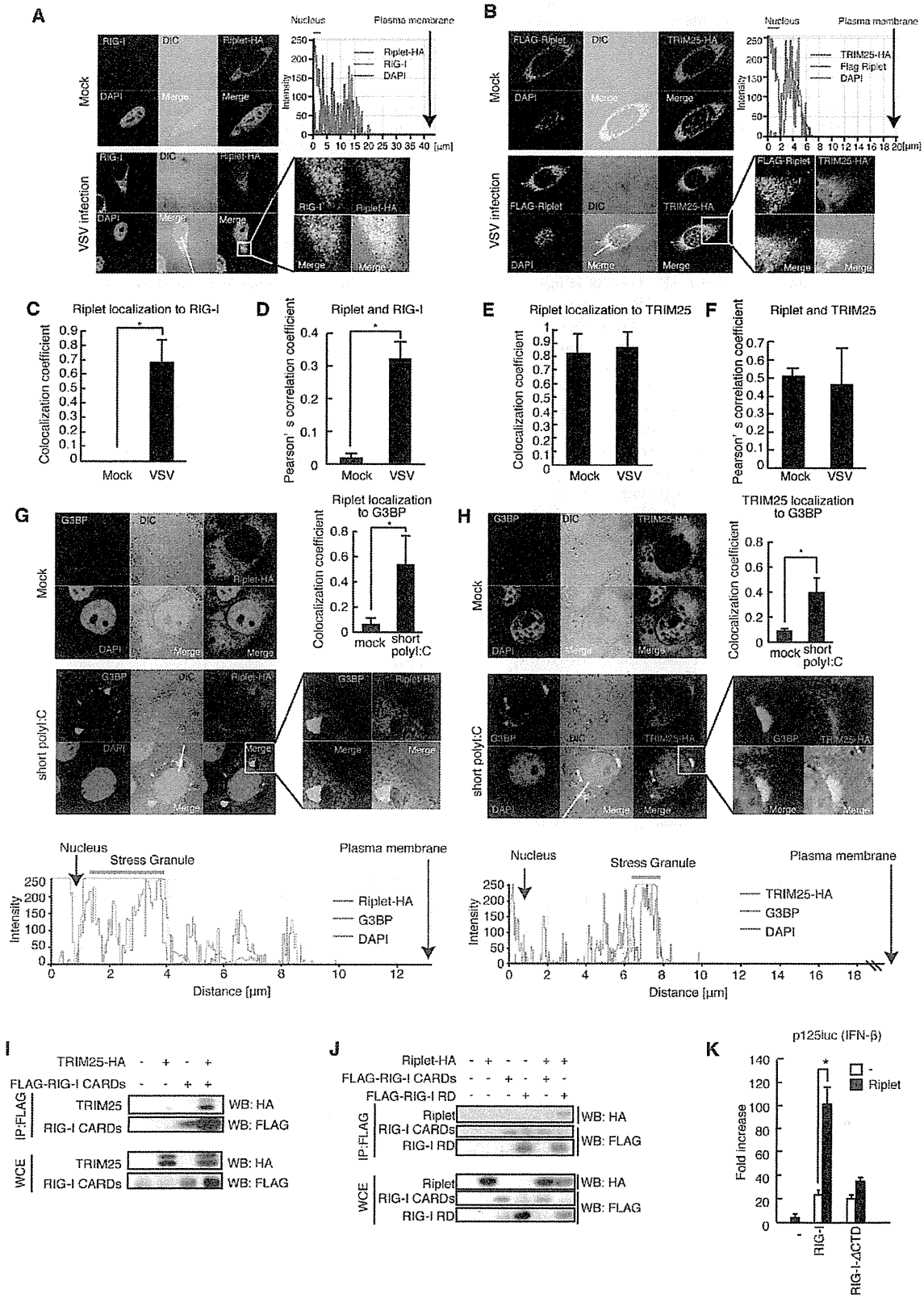
A
Mock
VSV infection
RIG-I
DIC
Riplet-HA
DAPI
Merge
Nucleus
Plasma membrane
Riplet-HA
RIG-I
DAPI
Intensity
B
FLAG-Riplet
TRIM25-HA
TRIM25-HA
Flag Riplet
C
Riplet localization to RIG-I
Colocalization coefficient
Mock
VSV
D
Riplet and RIG-I
Pearson' s correlation coefficient
E
Riplet localization to TRIM25
F
Riplet and TRIM25
G
G3BP
Riplet localization to G3BP
mock
short polyI:C
H
TRIM25 localization to G3BP
Stress Granule
Distance [μm]
I
TRIM25-HA
FLAG-RIG-I CARDs
IP:FLAG
WCE
TRIM25
RIG-I CARDs
WB: HA
WB: FLAG
J
Riplet-HA
FLAG-RIG-I RD
Riplet
RIG-I RD
K
p125luc (IFN-β)
Fold increase
RIG-I
RIG-I-ΔCTD

Figure 2. Riplet and TRIM25 ubiquitin ligases associate with RIG-I. (A, B) HeLa cells were transfected with Riplet-HA expression vector (A) or FLAG-Riplet and TRIM25-HA (B). 24 hours after transfection, the cells were infected with VSV at MOI = 1 for six hours. The cells were fixed and stained with anti-RIG-I (Alme-1), HA, and/or FLAG antibodies as indicated. Histograms display the measured fluorescence intensity along the white line in the merged panels. (C–F) Colocalization coefficients of Riplet localization to RIG-I (C) or TRIM25 (E) in mock or VSV infected HeLa cells. Pearson's correlation coefficient of Riplet and RIG-I (D) and TRIM25 (F) (mean ± SD, n>10). (G, H) HeLa cells were transfected with Riplet-HA (G) or TRIM25-HA (H) expression vector. The cells were stimulated with 100 ng of short poly(I:C) for six hours. The cells were fixed and stained with anti-G3BP and HA antibodies. Colocalization coefficient indicates values (mean ± SD, n>10) of Riplet (G) or TRIM25 (H) localization to G3BP staining region. Histograms display the measured fluorescence intensity along the white line in the merged panels. (I, J) TRIM25 (I) or Riplet (J) expression vector was transfected into HEK293FT cells together with FLAG-tagged-RIG-I CARDs or -RIG-I RD expression vectors. Cell lysate was prepared at 24 hours after transfection, followed by immunoprecipitation with an anti-FLAG antibody. (K) Riplet, RIG-I, and/or RIG-I-ΔRD, which lacks RD, expression vector was transfected into HEK293 cell with p125luc reporter. Reporter activation was determined at 24 hours after transfection. Data are presented as mean ± SD (n = 3).
doi:10.1371/journal.ppat.1003533.g002

mutations reduced the RIG-I polyubiquitination (Figure 4E). RIG-I polyubiquitination in cells stimulated with HCV dsRNA was also reduced by the K788R mutation (Figure 4F). Lys-788 is located within the 55-amino acid region (747–801 aa) of RIG-I essential for RD autorepression of CARDs signaling [31] (Figure 4A). It is possible that the reduction of RIG-I ubiquitination by the mutations was caused by the defect of RIG-I other functions, such as RNA binding activity. However, Figure 3C showed that the RIG-I 5KR and K788R mutant proteins efficiently bound to dsRNA as wild-type RIG-I. This data weakened the above possibility.

Using the RIG-I mutants, we investigated whether Riplet releases RIG-I RD autorepression. Because Riplet ectopic expression activated full-length RIG-I signaling even in the absence of stimulation (Figure 1D), we could assess whether Riplet can remove RIG-I RD autorepression by Riplet ectopic expression study. Due to autorepression, full-length RIG-I expression weakly activates the signaling compared with RIG-I CARDs expression [31]. Riplet ectopic expression increased full-length RIG-I signaling to a level comparable to that of RIG-I CARDs signaling (Figure 5A), suggesting that Riplet released the autorepression. Moreover, the K788R substitution canceled this Riplet ectopic expression effect on RIG-I signaling (Figure 5A). This suggested that the K788R mutation abrogated the release of RIG-I RD autorepression but not RNA binding activity.

Expression of the RIG-I RD fragment is known to represses full-length RIG-I-mediated signaling [3]. Interestingly, Riplet ectopic expression removed the RD fragment repression effect on RIG-I signaling (Figure 5B). This Riplet expression effect was canceled by the K788R amino acid substitution within full-length RIG-I (Figure 5B).

MDA5 C-terminal region does not function as an RD, and thus ectopically expressed MDA5 induced IFN-β promoter activity irrespective of viral infection [3]. If Riplet ectopic expression released RIG-I RD autorepression, it is expected that RIG-I and Riplet co-expression will induce IFN-β promoter activity irrespective of viral infection. As expected, Riplet and RIG-I co-expression induced IFN-β promoter activity irrespective of SeV infection (Figure 5C). Taken together, these genetic data indicated that Riplet released RIG-I RD autorepression.

If Riplet is essential for the release of RIG-I RD autorepression, it is expected that Riplet expression will increase the interaction between RIG-I and TRIM25, because TRIM25 efficiently activated RIG-I CARDs but not full-length RIG-I (Figure 1C and 1D). To test this possibility, we examined the interaction between TRIM25 and RIG-I in the presence or absence of Riplet ectopic expression and found that Riplet expression increased the interaction between TRIM25 and RIG-I (Figure 5D and 5E). Moreover, this interaction was abolished by the K788R mutation (Figure 5F). These data were also consistent with our model that Riplet affects RIG-I RD autorepression rather than RNA binding activity of RIG-I.

If Riplet is essential for the release of RIG-I RD autorepression leading to the interaction between TRIM25 and RIG-I, it was expected that Riplet is essential for endogenous RIG-I K63-linked polyubiquitination that is mediated by both Riplet and TRIM25. To test this possibility, we investigated endogenous RIG-I K63-linked polyubiquitination in mouse spleen cells infected with SeV. Endogenous RIG-I K63-linked polyubiquitination was increased after SeV infection in wild-type splenocyte, however knockout of Riplet abrogated the endogenous K63-linked polyubiquitination of RIG-I after SeV infection (Figure 5G). Recently, it was reported that knockdown of Riplet strongly reduced endogenous RIG-I polyubiquitination in response to SeV infection in a mouse cell line Hepa 1.6 [32]. Based on our genetic and biochemical data in Figure 3–5, we concluded that Riplet affects RIG-I RD autorepression rather than the RNA binding activity.

Riplet is required for the formation of a hetero-protein complex of RIG-I, TBK1, and IKK-ε

Because Riplet-mediated release of RD autorepression increased the interaction between RIG-I and TRIM25, we investigated whether the release of RD autorepression also increased the interaction of RIG-I with other factors. Interestingly, we found that ectopically expressed IKK-ε, TBK1, and NEMO ubiquitin binding region co-immunoprecipitated with RIG-I RD (Figure 6A–6D), and Riplet expression enhanced the physical interactions of RIG-I with TBK1, IKK-ε, and the NEMO ubiquitin binding region (Figure 6D–6G). The physical interactions between these proteins were not through IPS-1, as IPS-1 did not co-immunoprecipitate with RIG-I RD (Figure 6B).

Microscopy analysis showed that the RIG-I was co-localized with TBK1 or NEMO in the cytoplasm. (Figures 6H and S2A). RIG-I and TBK1 was detected in the region where there is no mitochondria (Figure 6I), and the colocalization of RIG-I with TBK1 was also detected in the region where there is no mitochondria (yellow stained region in Figure 6J). This was consistent with our immunoprecipitation results that RIG-I RD could bind TBK1 without IPS-1. TBK1 is phosphorylated in its activation loop [33]. Surprisingly, the phosphorylated TBK1 (p-TBK1) foci were exclusively localized on mitochondria (Figure 6K and 6L). Co-localization of RIG-I with p-TBK1 was observed after dsRNA stimulation (Figure S2B and S2C). We next assessed the role of endogenous Riplet in the interaction between RIG-I and TBK1. Immunoprecipitation assay showed that Riplet KO reduced the interaction between endogenous RIG-I and TBK1 in mouse spleen cells during VSV infection, indicating that Riplet promoted the interaction between RIG-I and TBK1 (Figure 6M). These data indicated that the Riplet function increased the interaction of RIG-I with TBK1 as well as TRIM25.

Hepatitis C virus protease NS3-4A targets the Riplet protein

Several viruses have evolved strategies to escape the innate immunity. For instance, NS1 of influenza A virus inhibits TRIM25 function. This emphasizes the vital role of TRIM25 in

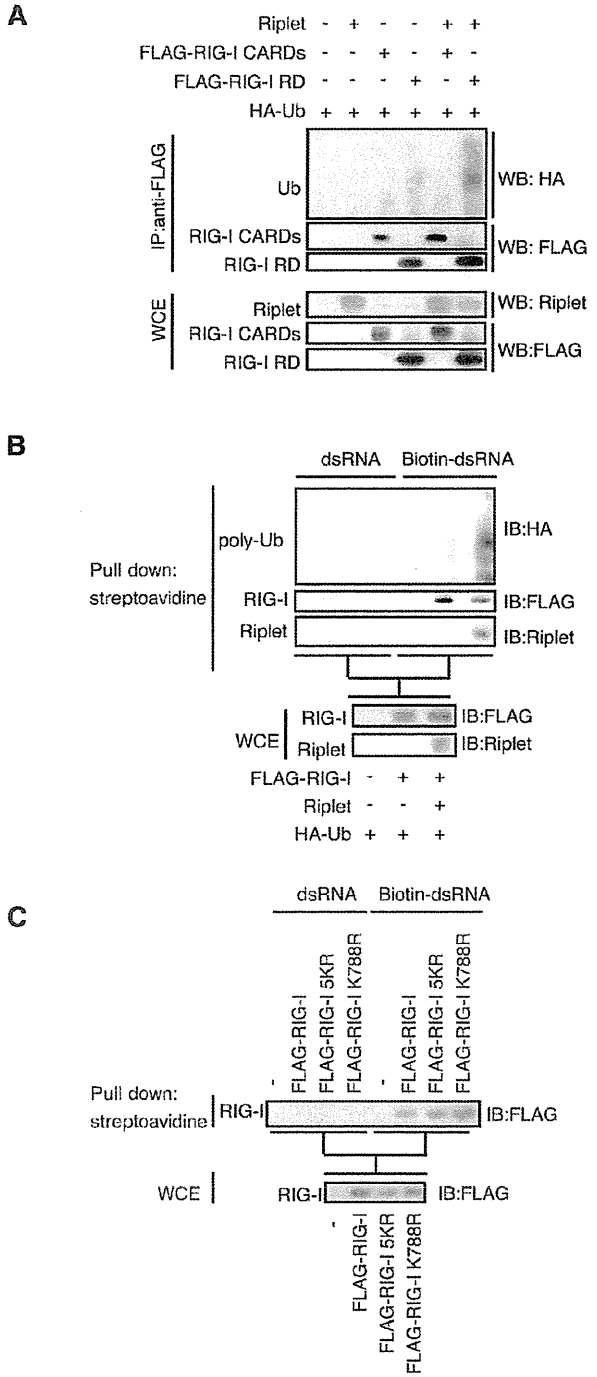

Figure 3. Riplet function is dispensable for RIG-I RNA binding activity. (A) Expression vectors encoding Riplet, FLAG-tagged RIG-I CARDs, and/or FLAG-tagged RIG-I RD were transfected into HEK293FT cells together with an HA-tagged ubiquitin expression vector. Cell lysate was prepared at 24 hours after transfection, followed by immunoprecipitation with an anti-FLAG (RIG-I) antibody. (B) HEK293FT cells were transfected with expression vectors encoding FLAG-tagged RIG-I, Riplet, and HA-tagged ubiquitin. Cell lysate was prepared at 24 hours after transfection, and then incubated with biotin-conjugated (Biotin-dsRNA) or non-conjugated (dsRNA) double-stranded RNA. Biotin-dsRNA was pull-downed with streptavidin beads. Samples were subjected to SDS-PAGE, and proteins were detected by western blotting. (C) HEK293FT cells were transfected with FLAG-tagged wild-type RIG-I, RIG-I 5KR, or RIG-I K788R expression vector. 24 hours after the transfection, the cell lysate was prepared. The pull down assay with biotin-dsRNA was performed as described above.
doi:10.1371/journal.ppat.1003533.g003

modulating antiviral response [34]. To assess the biological significance of Riplet-mediated release of RIG-I RD autorepression in antiviral innate immune response, we investigated whether viral protein suppresses this mechanism.

The endogenous Riplet protein level was not affected by polyI:C, HCV dsRNA stimulations, or by VSV infection (Figure 7A–7C), however the Riplet protein level was severely reduced in a human hepatocyte cell line with HCV 1b full-length replicons (O cells) compared with hepatocyte cell line without these replicons (O curred cells: Oc cells; Figure 7D), suggesting that viral protein reduced the Riplet protein level. Riplet knockout abolished the expression of type I IFN, IP-10, and type III IFN in response to HCV RNA (Figure 7E), indicating that Riplet was essential for type I IFNs expression in response to HCV RNA.

Because HCV protease NS3-4A suppresses type I IFN expression in response to viral infection [7,25], we examined whether NS3-4A could cleave the Riplet protein. N-terminal FLAG-tagged Riplet or C-terminal HA-tagged Riplet was expressed with or without NS3-4A, after which the Riplet protein levels were compared. NS3-4A expression severely reduced the FLAG-tagged and HA-tagged Riplet protein level but not that of FLAG-tagged RIG-I, whereas catalytically inactive NS3-4A* (S139A) failed to reduce the Riplet protein level (Figure 7F, 7G, and S3A). This suggested that this protease's activity reduced the Riplet protein level. Although NS3-4A reduced IPS-1 protein level as previously reported, NS3-4A did not reduce the TRIM25 and IKK-ε protein levels (Figure 7H, 7I, S3B–D).

Within the Riplet RING-finger domain is a sequence that is similar to the NS3-4A target consensus sequence (D/E-x-x-x-x-C/T-S/A; Figure 7J) [35]. NS3-4A cleaves the target just after C/T within this consensus sequence. Acidic amino acids before the C/T site are conserved among the NS3-4A cleavage site within HCV polypeptide. The acidic amino acids from 16 to 18 aa within the Riplet sequence were substituted with Ala, and a Riplet-3A mutant protein was constructed (Figure 7J). The Riplet-3A mutant protein was resistant to NS3-4A (Figure 7I and 7K). Moreover, the Riplet-3A protein co-localized with NS3-4A in cytoplasm (Figure 7L). Interestingly, recombinant NS3-4A that was purified from *E. coli* cleaved the immunoprecipitated FLAG-tagged Riplet protein and recombinant GST-fused Riplet protein purified from *E.coli*, and the cleaved fragments were detected at expected size (Figure 7M and 7N). These data indicated that NS3-4A directly targeted the Riplet protein.

Although Riplet digestion products were not observed in HEK293 cell lysate (Figure S3E and S3F), it is known that the digestion products of TICAM-1 (TRIF) obtained by NS3-4A are not detectable because these products are unstable [28]. Cys-21 of Riplet corresponds to the C/T site in the NS3-4A target consensus sequence. The Cys-21 residue is the first Cys in the RING-finger motif; thus a C21A substitution causes the disruption of RING finger domain structure [36]. The Riplet-C21A mutant protein was unstable and barely detectable (Figure S3G), which suggested that the loss of Cys-21 destabilized the Riplet protein.

HCV protease NS3-4A abolishes an early step of RIG-I activation

To determine if NS3-4A abolishes RIG-I activation by disrupting Riplet, we examined RIG-I ubiquitination and

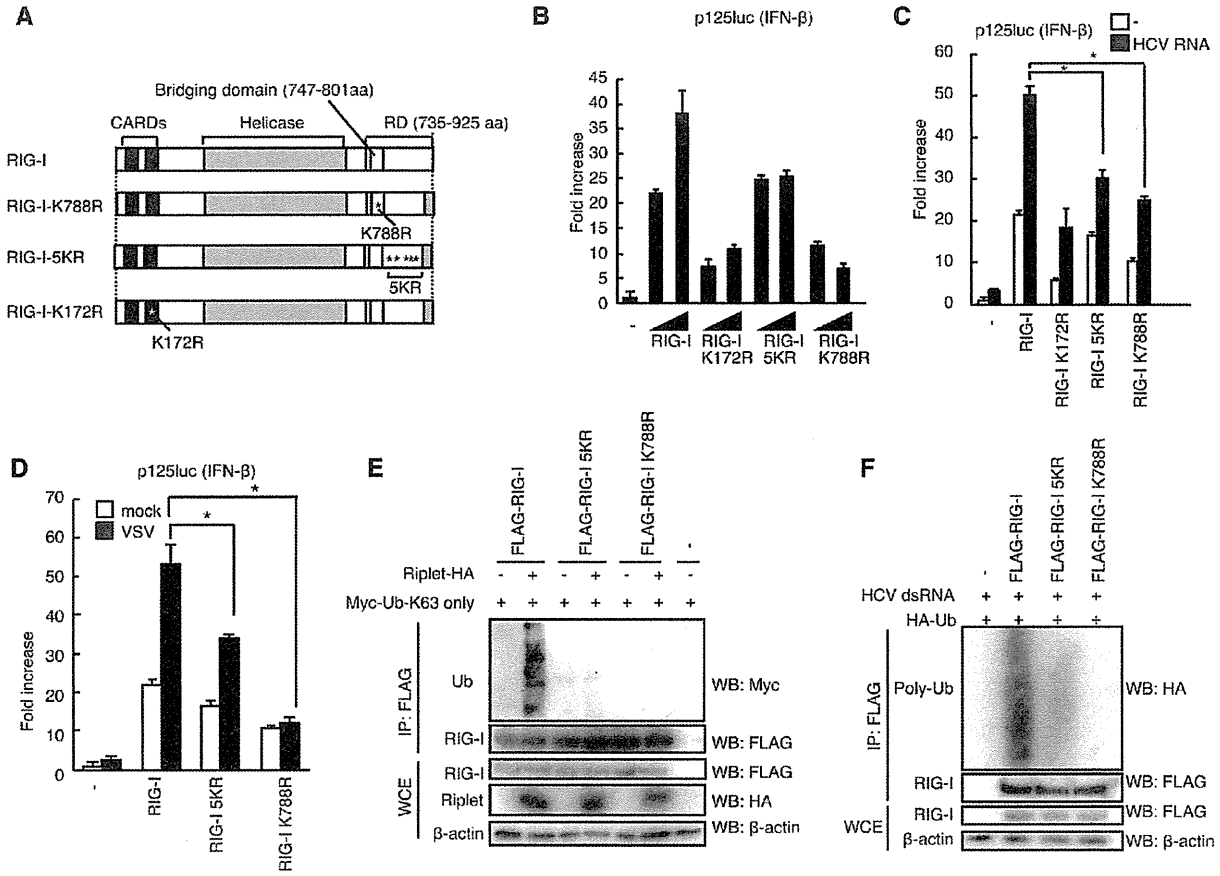

Figure 4. Lys residues within RIG-I RD were essential for Riplet-mediated K63-linked polyubiquitination. (A) Schematic diagram of RIG-I mutant proteins. (B–D) IFN-β promoter activation was determined using a p125luc IFN-β reporter gene. HEK293 cells were transfected with 0.1 μg of expression vectors encoding full-length RIG-I, RIG-I K172R, RIG-I 5KR, and RIG-I K788R in 24-well plate. The transfected cells were stimulated with 0.1 μg of HCV 3′ UTR dsRNA using lipofectamine 2000 reagent for eight hours (C) or infected with VSV at MOI = 1 for 24 hours (D), after which reporter activation was determined. Data are presented as mean ± SD (n = 3). *$p<0.05$. (E) The expression vectors encoding HA-tagged Riplet and FLAG-tagged RIG-I, RIG-I 5KR, and RIG-I K788R were transfected into HEK293FT cells together with Myc-tagged K63-only ubiquitin expression vector, in which all Lys residues except Lys-63 within ubiquitin were replaced with Arg. At 24 hours after transfection, cell lysates were prepared, followed by immunoprecipitation with an anti-FLAG (RIG-I) antibody. (F) The expression vectors encoding FLAG-tagged wild-type and mutant RIG-I proteins were transfected into HEK293FT cells together with HA-tagged ubiquitin expression vector. 24 hours after the transfection, the cells were stimulated with HCV 3′ UTR dsRNA by transfection for eight hours. Then cell lysate was prepared and immunoprecipitation was performed with anti-FLAG antibody.
doi:10.1371/journal.ppat.1003533.g004

interaction between RIG-I and TRIM25. Riplet-mediated ubiquitination of full-length RIG-I or RIG-I RD was abolished by NS3-4A expression (Figure 8A and 8B). K63-linked polyubiquitination of RIG-I RD in SeV infected cells were also reduced by NS3-4A expression (Figure 8C). Moreover, NS3-4A expression reduced the interaction between TRIM25 and full-length RIG-I (Figure 8D).

An IPS-1-C508A mutant protein is resistant to NS3-4A cleavage [7]. A reporter gene assay showed that NS3-4A expression severely reduced IFN-β promoter activation induced by RIG-I and Riplet expression even in the presence of the IPS-1 C508A mutant protein in HEK293 cell (Figure 9A), and a catalytically inactive NS3-4A mutant failed to reduce this signal (Figure 9B). These data were consistent with our observation that NS3-4A targeted the Riplet protein. There was endogenous IPS-1 in HEK293 cell, and thus the decrease of IFN-β promoter induction by NS3-4A in HEK293 cell could be due to the cleavage of endogenous IPS-1 by NS3-4A. To exclude this possibility, we next used IPS-1 KO mouse hepatocyte [37]. The IPS-1 C508A mutant protein was expressed in IPS-1 KO hepatocyte. NS3-4A expression reduced the reporter activation induced by RIG-I/Riplet expression or by stimulation with HCV dsRNA even in the presence of IPS-1 C508A (Figure 9C and 9D). These results indicated that NS3-4A targeted both IPS-1 and upstream factors of IPS-1 and were consistent with our observation that NS3-4A reduced the Riplet protein level. We could not test whether NS3-4A failed to impair IFN-β promoter activity in the presence of the Riplet-3A and Riplet C21A mutants because the mutant proteins were not functional and failed to activate RIG-I (Supplemental Figure S3H and S3I). Thus, we could not exclude the possibility that NS3-4A targeted another protein in addition to Riplet and IPS-1.

Hepatitis C virus abrogates endogenous Riplet function

Endogenous RIG-I exhibited punctate staining in the human hepatocyte cell line HuH7 and HepG2 cells after simulation with